

Article

Sensitivity of Summertime Convection to Aerosol Loading and Properties in the United Arab Emirates

Ricardo Fonseca ¹, Diana Francis ^{1,*}, Michael Weston ¹, Narendra Nelli ¹, Sufian Farah ², Youssef Wehbe ², Taha AlHosari ², Oriol Teixido ³ and Ruqaya Mohamed ³

¹ The Environmental and Geophysical Sciences (ENGEOS) Lab, Khalifa University of Science and Technology, Abu Dhabi P.O. Box 127788, United Arab Emirates; ricardo.fonseca@ku.ac.ae (R.F.); Michael.Weston@ku.ac.ae (M.W.); narendra.nelli@ku.ac.ae (N.N.)

² National Center for Meteorology (NCM), Abu Dhabi P.O. Box 4815, United Arab Emirates; SFarrah@ncms.ae (S.F.); YWehbe@ncms.ae (Y.W.); TAlhosary@ncms.ae (T.A.)

³ Environment Agency—Abu Dhabi (EAD), Abu Dhabi P.O. Box 45553, United Arab Emirates; oriol.teixido@ead.gov.ae (O.T.); ruqaya.mohamed@ead.gov.ae (R.M.)

* Correspondence: diana.francis@ku.ac.ae

Abstract: The Weather Research and Forecasting (WRF) model is used to investigate convection–aerosol interactions in the United Arab Emirates (UAE) for a summertime convective event. Both an idealized and climatological aerosol distributions are considered. The convection on 14 August 2013 was triggered by the low-level convergence of the cyclonic circulation associated with the Arabian Heat Low (AHL) and the daytime sea-breeze circulation. Numerical experiments reveal a high sensitivity to aerosol properties. In particular, replacing 20% of the rural aerosols by carbonaceous particles has a comparable impact on the surface radiative fluxes to increasing the aerosol loading by a factor of 10. In both cases, the UAE-averaged net shortwave flux is reduced by $\sim 90 \text{ W m}^{-2}$ while the net longwave flux increases by $\sim 51 \text{ W m}^{-2}$. However, when the aerosol composition is changed, WRF generates 20% more precipitation than when the aerosol loading is increased, due to a broader and weaker AHL. The surface downward and upward shortwave and upward longwave radiation fluxes are found to scale linearly with the aerosol loading. An increase in the amount of aerosols also leads to drier conditions and a delay in the onset of convection due to changes in the AHL.

Keywords: convection; cold pools; aerosol loading; numerical modelling; aerosol properties



Citation: Fonseca, R.; Francis, D.; Weston, M.; Nelli, N.; Farah, S.; Wehbe, Y.; AlHosari, T.; Teixido, O.; Mohamed, R. Sensitivity of Summertime Convection to Aerosol Loading and Properties in the United Arab Emirates. *Atmosphere* **2021**, *12*, 1687. <https://doi.org/10.3390/atmos12121687>

Academic Editor: Alexandros Papayannis

Received: 8 November 2021

Accepted: 13 December 2021

Published: 16 December 2021

Publisher's Note: MDPI stays neutral with regard to jurisdictional claims in published maps and institutional affiliations.



Copyright: © 2021 by the authors. Licensee MDPI, Basel, Switzerland. This article is an open access article distributed under the terms and conditions of the Creative Commons Attribution (CC BY) license (<https://creativecommons.org/licenses/by/4.0/>).

1. Introduction

It has long been known that aerosols, defined as solid or liquid particles suspended in the atmosphere from both from natural and anthropogenic sources, play an important role in the climate system [1–3]. Aerosols significantly interact both with the radiation (direct and semi-direct effects; [4–6]) and cloud microphysics (indirect effects; [7]). For simplicity, the former will be denoted as aerosol–radiation interactions (ARI) and the latter as aerosol–cloud interactions (ACI) throughout the text. Aerosols scatter and absorb solar (shortwave) and thermal (longwave) radiation, leading to a warming of the aerosol layer and a cooling of the surface below. As far as the ACI effects are concerned, an increase in aerosol loading leads to a larger number of smaller cloud droplets (first indirect or Twomey effect), which leads to more scattering and hence a higher cloud albedo and optical depth [8]. As a result, aerosols act to suppress precipitation, increasing the cloud lifetime and cloud height (second indirect or Albrecht effect; [9]). While pollution and smoke from industrial activities are the most common anthropogenic aerosols, dust is the most abundant natural aerosol on Earth. The Sahara Desert is the main source region of mineral dust, accounting for roughly half of global dust emissions [10], with contributions from other hyperarid regions such as the Arabian Desert in the Middle East [11], the Gobi Desert in East Asia, and the Sonoran Desert in the United States [12]. Dust has been shown

to have an important impact on the climate system, in particular on the atmosphere [13–15], ocean [16] and cryosphere [11] dynamics.

The direct and indirect effects of dust aerosols on convection are discussed in [17] for a Mesoscale Convective System (MCS) that was developed over North Africa in July 2010 using the Weather Research and Forecasting (WRF; [18]) model. The authors found that the ACI effects initially weaken the convective system, due to the slowdown of the conversion rate from cloud to rain and subsequent suppression of warm rain formation, but later strengthen it, as dust acts as condensation nuclei and increases the number of hydrometeors. In the end, switching on the ACI effects leads to a roughly 18% increase in precipitation. The ARI effects are found to have the largest influence on the development of convection in dusty areas, leading to a stronger, albeit delayed, MCS. This is because the heating of the dust layer during the day reduces convective instability, but the increase in downward longwave radiation flux at the surface [19] will ultimately lead to higher instability and a roughly 14% increase in precipitation. When the ACI is added, the MCS intensifies further, with an increase in total rainfall as high as 39% during the first convective development cycle. This figure is larger than the sum of the precipitation increase when the ARI and ACI effects are switched on separately, which is evidence of a non-linear interaction of the two effects. In [20], the WRF model was used with Chemistry (WRF-Chem; [21]) to investigate the effects of biomass-burning aerosols on radiation, clouds and precipitation in the Amazon basin. The authors found that the ACI effects prevailed at lower emission rates and low values of aerosol optical depth (AOD), while the ARI effects played the largest role at high emission rates and high AODs. The authors in [22] tested the sensitivity of the WRF response to anthropogenic and mineral dust emissions over the Sahara for July 2016. They concluded that a doubling of the amount of dust led to a 0.5 K and 25 m decrease in the 2 m temperature and the planetary boundary layer (PBL) depth, respectively. The surface net shortwave and longwave radiation fluxes changed by up to 25 W m^{-2} , the former decreasing and the latter increasing. When the model predictions are evaluated against observations, some authors found that accounting for the ACI and ARI effects clearly improves the accuracy of the forecasts (e.g., [23] for a rainfall event in India), while others reported a smaller impact (e.g., [24] for a summertime convective event in Serbia). Adding the effects of aerosols also improves the model representation of clouds, for both ice- and liquid-water-related quantities [25,26].

The United Arab Emirates (UAE) is a country located in the Middle East, bounded by the Arabian Gulf to the north and west, the Sea of Oman to the northeast, and the Rub' Al Khali desert to the south. The country is rather flat, except in the northeastern side where the Al Hajar mountain range dominates the landscape (see Figure 1), with the highest elevation of around 2000 m at Jabel Jais. The meager and irregular amounts of precipitation, with annual totals ranging from less than 40 mm in the southern desert to over 120 mm over the mountains, mostly fall in the cold season from November to March, in association with mid-latitude weather systems [27–29]. However, summertime convective events also occur, and can lead to rainfall accumulations of more than 50 mm day^{-1} and flash floods at isolated sites [19,30–32].

Convection in the UAE in the warm season normally takes place on the eastern side around the Al Hajar mountains. As discussed in [31,34], it is triggered by the convergence of the low-level circulation associated with the Arabian Heat Low (AHL; [35,36]), the sea-breeze circulation from the Arabian Gulf and Sea of Oman, and the upslope flows on the mountains. The presence of a mid- to upper-level trough and associated unstable stratification also promotes the development of convective clouds [19]. Although less frequent, convective events also take place in the flatter western half. Here, they are commonly triggered by the low-level convergence of the AHL and sea-breeze circulations [30]. The AHL's strength is modulated by the Indian Summer Monsoon [30] and sea surface temperatures (SSTs) in the Indian Ocean [37] and in the equatorial Pacific [35]. A stronger AHL, typically seen during periods of enhanced convective activity over the Arabian Sea when the increased descent and subsidence over the Arabian Peninsula helps to intensify the

heat low, modulates the inland penetration of the marine boundary layer. The convergence line between the moister marine air and the hotter and drier desert air, which plays an important role in the triggering of dust [38,39] and convective [19] storms, is labelled as the Intertropical Discontinuity (ITD). Its position is therefore linked to the strength and spatial extent of the AHL, as explained in [35].

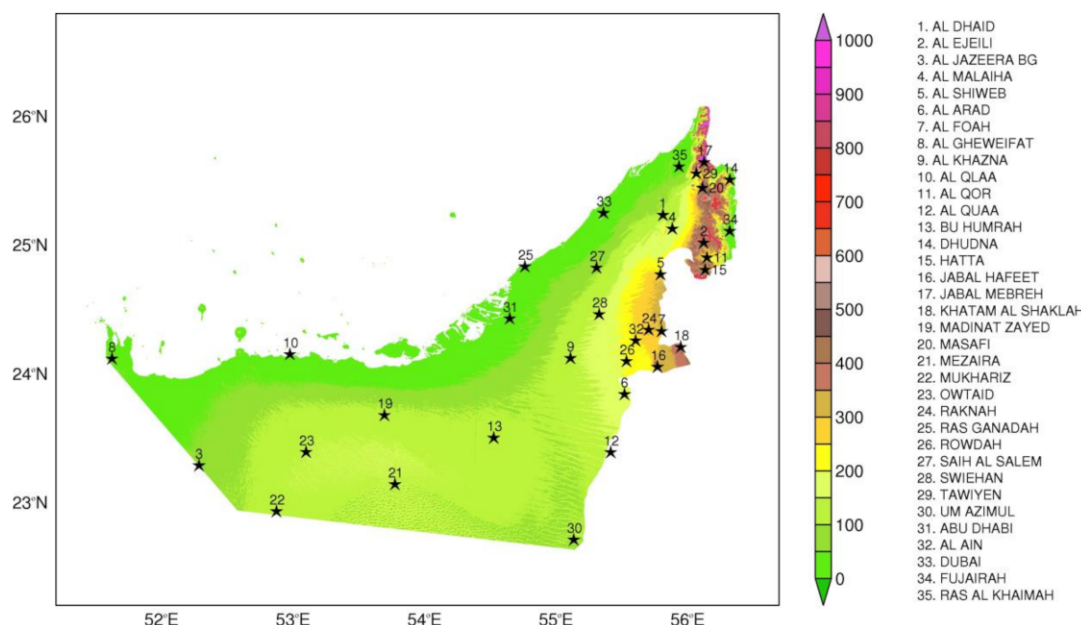


Figure 1. Location and name of NCM’s 30 automatic weather stations (1–30) and 5 airport stations (31–35) for which weather measurements were available on 14 August 2013. The United Arab Emirates’ orography was taken from a 30 m digital elevation model [33].

Being part of the Arabian Desert, aerosols are ubiquitous in the UAE. As discussed in [40], the prevailing aerosol subtype is dust, with higher AODs in summer and spring, typically in the range 0.3–0.6. During dust storms, the AOD can exceed the climatological values by an order of magnitude; for example, during the July 2018 event, it exceeded 3 with more than 20×10^{15} g or 20 Tg of dust being lifted into the atmosphere [11]. On diurnal scales, the AOD values are slightly higher in the early morning when the nighttime low-level jet mixes down to the surface, with the stronger near-surface winds lifting higher amounts of dust [41]. The aerosol variability in the UAE is also discussed in [42], which analyses measurements collected by a LIDAR from February 2018 to February 2019. The authors concluded that the size of the aerosols is more important than their chemistry (i.e., composition, which affects the hygroscopicity) for aerosol particle activation, in line with the findings of [43].

In this work, the interaction between aerosols and convection in the UAE is investigated for a summertime convective event that occurred on a relatively dusty day. The two main objectives of this study are as follows: (i) investigate the added value of incorporating aerosols and accounting for their direct and indirect effects on the model-predicted convective activity, and (ii) explore the sensitivity of the WRF response to different aerosol loadings and properties and assess how it compares against observations. The findings of this work will be very relevant to other arid/hyperarid regions, in particular those adjacent to major aerosol sources, such as deserts.

This paper is structured as follows. In Section 2, a description of the model, datasets and numerical simulations conducted is given. The meteorological conditions on 14 August 2013, the event targeted in this work, are analysed in Section 3. In Section 4, the results of the model simulations are discussed, with the main findings outlined in Section 5.

2. Materials and Methods

2.1. Numerical Model

The numerical model used in this study is the WRF model version 4.2.1 [18]. WRF is a fully compressible, non-hydrostatic, community model, which makes use of the Arakawa-C grid staggering for horizontal discretization and employs the Lorenz grid for vertical discretization. In all simulations, WRF is initialized on 13 August 2013 and run for 48 h, with the first 24 h discarded as model spin-up. As discussed in Section 3, the 14 August 2013 convective event is selected as it features both deep convection and a dusty atmosphere over the UAE. The initial and boundary conditions are taken from ERA-5 data [44], the latest reanalysis dataset of the European Center for Medium Range Weather Forecasts, which provides meteorological fields on a $0.25^\circ \times 0.25^\circ$ grid and on an hourly basis, from 1979 to present. WRF model experiments are run in a three-nest configuration, with spatial resolutions of 22.5 km, 7.5 km and 2.5 km. The spatial extent of the model grids is presented in Figure 2a. The outermost grid is at a resolution of 22.5 km, and covers the vast majority of the Arabian Peninsula and surrounding region, while the innermost nest, at 2.5 km resolution, is centered over the UAE and extends into the adjacent Arabian Gulf and Sea of Oman (Figure 2b). The boundary conditions from ERA-5 are relaxed on a five grid-point buffer zone (not displayed in Figure 2a,b). The grid resolutions used here are the same as those employed in [19] for the 5 September 2017 convective event in the UAE. In that study the authors concluded that adding another nest, at a spatial resolution of 0.833 km, does not provide added value to the model forecasts.

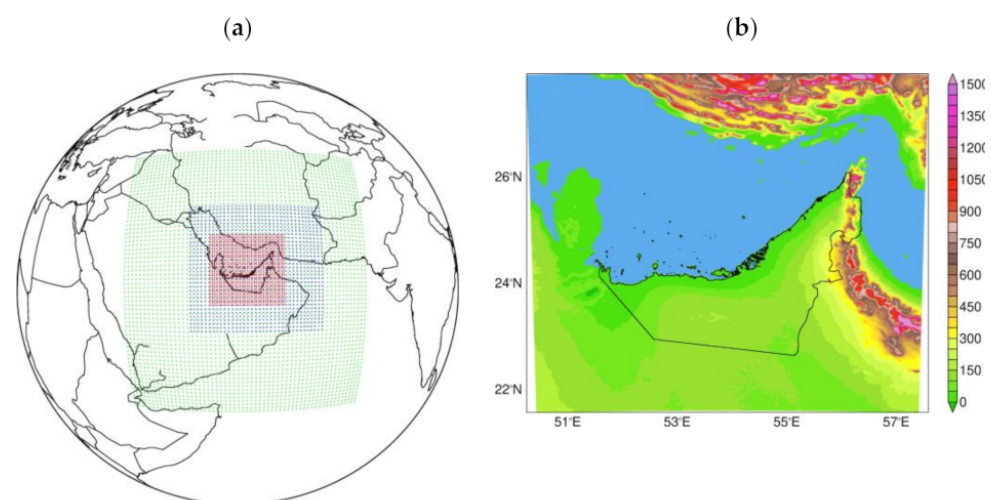


Figure 2. (a) Spatial extent of the WRF's 22.5 km (green), 7.5 km (blue) and 2.5 km (red) grids used in the experiments. (b) Zoomed-in view of the 2.5 km grid, with the shading giving the orography as seen by the model (m).

The physics schemes employed in the WRF simulations are summarized in Table 1. The model set up reflects the findings of [34], who tested different WRF configurations for the 14 July 2015 convective event in the UAE. The authors in [34] noted that a 0.025° grid (~ 2.7 km) may still be too coarse to represent shallow clouds, and hence they employed a shallow cumulus scheme in their runs. The same applies to the 2.5 km grid considered here, and for that purpose the mass-flux scheme embedded in the MYNN PBL scheme, which parametrizes the non-convective component of the subgrid clouds [45], was activated. The Noah-MP is configured following [19,46], while the sea surface skin temperature scheme of [47], which allows for the simulation of its diurnal cycle and feedback on the atmosphere, is switched on. In the vertical, 45 levels are considered, more closely spaced in the PBL, with the first level at about 27 m above the ground, and with the model top at 50 hPa. Rayleigh damping is applied in the top 5 km to the wind components and potential temperature and on a timescale of 5 s to damp vertically propagating waves [18]. In all simulations,

the more realistic representation of the soil texture and land use land cover over the UAE described in [48] is employed.

Table 1. Physics schemes employed in the WRF simulations.

Parameterization Scheme	Option
Cloud Microphysics	Thompson–Eidhammer scheme [49] (In the default version, only ACI effects are activated; ARI effects are switched on through an option in the model’s namelist)
Planetary Boundary Layer (PBL)	Mellor–Yamada Nakanishi Niino (MYNN) level 2.5 [50,51], with mass-flux scheme [45] activated
Radiation	Rapid Radiative Transfer Model for Global Circulation Models [52]
Cumulus	22.5 km and 7.5 km grids: Kain–Fritsch [53], with subgrid-scale cloud feedbacks to radiation [54] 2.5 km grid: no cumulus scheme
Land Surface Model (LSM)	Noah LSM with MultiParameterization options [55,56]
Sea Surface Temperature (SST)	6-hourly ERA-5 SSTs + simple skin temperature scheme [47]

2.2. WRF Experiments

A total of nine WRF simulations were performed, as listed in Table 2. The main difference between them is in the set-up of the Thompson–Eidhammer cloud microphysics scheme. This scheme, also known as Thompson aerosol-aware, is a modified version of the original Thompson scheme [57,58], incorporating the activation of aerosols as cloud condensation nuclei and ice nuclei in a simplified manner [49]. Two new variables, representing the concentration of hygroscopic or “water-friendly” aerosols (N_{wfa} ; designed to account for a combination of sulfates, sea salts, and organic matter) and non-hygroscopic or “ice-friendly” aerosols (N_{ifa} ; mineral dust), are added to the model. Aerosol direct and semi-direct effects, namely the scattering and absorption of radiation [59], as well as indirect effects, aerosol–cloud interactions [60], can be accounted for in a relatively computationally cheap way, when compared, e.g., to the simplest set up of the WRF-Chem [21] as noted by [61]. It is important to stress that in the default version of the scheme only ACI effects are activated; the ARI effects are switched on through an option in the model’s namelist which allows the radiation scheme to “see” the N_{wfa} and N_{ifa} populations as discussed below.

Table 2. List of the WRF simulations discussed in this study. The experiments differ in the aerosol profile considered (idealized profile, IDEAL, or climatological profile, CLIM, the latter scaled by a factor of 5 in experiments number 6–8, and 10 in experiment number 9), aerosol–radiation interactions (ARI) option (rural, urban and maritime models), and whether grid nudging is applied in the two outermost model grids (NUDGE).

Numerical Experiment	Aerosol Profile	ARI Setting	Nudging
1. WRF-IDEAL	IDEAL	-	-
2. WRF-IDEAL-ARI_R	IDEAL	RURAL	-
3. WRF-CLIM	CLIM	-	-
4. WRF-CLIM-ARI_R	CLIM	RURAL	-
5. WRF-CLIM-ARI_R-NUDGE	CLIM	RURAL	NUDGE
6. WRF-5×CLIM-ARI_R-NUDGE	5×CLIM	RURAL	NUDGE
7. WRF-5×CLIM-ARI_U-NUDGE	5×CLIM	URBAN	NUDGE
8. WRF-5×CLIM-ARI_M-NUDGE	5×CLIM	MARITIME	NUDGE
9. WRF-10×CLIM-ARI_R-NUDGE	10×CLIM	RURAL	NUDGE

There are two ways to initialize the aerosol concentration arrays: (i) employing an idealized profile based on prescribed concentrations and the terrain height (IDEAL); (ii) extracting the aerosol profiles from a 7-year (2001–2007) simulation with the Goddard Chemistry Aerosol Radiation and Transport (GOCART; [62]) model, described in [63] (CLIM).

In (i), where idealized aerosol profiles are used, the aerosol concentration is defined as

$$N(z) = N_1 + N_0 \text{EXP} \left[- \left(\frac{h(z) - h(1)}{1000} \right) N_3 \right] \quad (1)$$

with

$$N_3 = -\frac{1}{0.8} \text{LOG} \left(\frac{N_1}{N_0} \right) \text{ if } h(1) \leq 1000 \text{ m} \quad (2)$$

$$N_3 = -\frac{1}{0.01} \text{LOG} \left(\frac{N_1}{N_0} \right) \text{ if } h(1) \geq 2500 \text{ m} \quad (3)$$

$$N_3 = -\frac{1}{0.8 \text{COS} [h(1) \times 0.001 - 1]} \text{LOG} \left(\frac{N_1}{N_0} \right) \text{ if } 1000 \text{ m} < h(1) < 2500 \text{ m} \quad (4)$$

In the equations above, $h(z)$ is the height of the model level z in meters, with $h(1)$ being the height of the first model level. The constants N_1 and N_0 are set to $50 \times 10^6 \text{ m}^3$ and $300 \times 10^6 \text{ m}^3$ for water-friendly aerosols, and $0.5 \times 10^6 \text{ m}^3$ and $1.5 \times 10^6 \text{ m}^3$ for ice-friendly aerosols, respectively. This definition is based on the premise that aerosols are mostly concentrated in the lowest part of the atmosphere, with a faster decrease with height over the higher terrain, and a profile tailored for the continental United States. Spatially, N_{wfa} and N_{ifa} are uniform at the start of the run, but evolve during the course of the model integration.

In (ii), the climatological aerosol distribution used to initialize the aerosol fields is that described in [49]. It is a $0.5^\circ \times 1.25^\circ$ dataset available on a monthly timescale and on 30 vertical levels, comprising both water-friendly (sulphates, sea salts and organic carbon) and ice-friendly (dust, with particle sizes larger than $0.5 \mu\text{m}$) aerosols. This dataset is generated from a global model simulation, with the predicted aerosol optical depth and Angstrom exponent comparing well with those estimated from satellite data in particular in this region [63].

As discussed in [49], and for the “ice-friendly” aerosols in more detail in [25], the temporal evolution of N_{wfa} and N_{ifa} is given by Equations (5) and (6) below.

$$\begin{aligned} \frac{dN_{wfa}}{dt} = & - \left(\begin{array}{c} \text{rain, snow, graupel} \\ \text{collecting aerosols} \end{array} \right) - \left(\begin{array}{c} \text{homogeneous nucleated} \\ \text{deliquesced aerosols} \end{array} \right) \\ & - (\text{CCN activation}) \\ & + \left(\begin{array}{c} \text{cloud and rain} \\ \text{evaporation} \end{array} \right) + \left(\begin{array}{c} \text{surface} \\ \text{emissions} \end{array} \right) \end{aligned} \quad (5)$$

$$\begin{aligned} \frac{dN_{ifa}}{dt} = & - \left(\begin{array}{c} \text{rain, snow, graupel} \\ \text{collecting aerosols} \end{array} \right) - (\text{IN activation}) + \left(\begin{array}{c} \text{cloud ice} \\ \text{sublimation} \end{array} \right) \\ & + \left(\begin{array}{c} \text{surface} \\ \text{emissions} \end{array} \right) \end{aligned} \quad (6)$$

where CCN stands for Cloud Condensation Nuclei and IN for Ice Nuclei. The source terms for both the “water-friendly” and “ice-friendly” aerosols can be summarized as follows:

1. The nucleation of cloud droplets from N_{wfa} is achieved through a lookup table with the activation fraction as a function of parameters such as the WRF-predicted temperature, updraft speed, number of available aerosols, and predefined values of the hygroscopicity parameter and the aerosol’s mean radius;
2. Once nucleated, the aerosols are removed from N_{wfa} , the third term on the right-hand-side (RHS) of Equation (5), but can be restored via hydrometeor evaporation,

- the fourth term in Equation (5). Aerosols can also be removed from the population by precipitation scavenging, the first term in Equations (5) and (6);
3. For “water-friendly” aerosols, and when a climatological-based distribution is employed, a constant surface emission forcing is added in the lowest model layer based on the starting near-surface aerosol concentration. A similar contribution is not considered for the “ice-friendly” aerosols in the present version of the scheme, i.e., the last term on the RHS of Equation (6) is set to zero;
 4. The nucleation of dust particles into ice crystals occurs in the presence of supersaturation with respect to ice. Depending on the relative humidity (RH) with respect to water, condensation, immersion freezing (i.e., ice nucleation by particles immersed in supercooled water) and deposition nucleation (i.e., formation of ice from supersaturated water vapor on an insoluble particle without prior formation of liquid) can occur. These processes are accounted for by the second term on the RHS of Equation (6);
 5. The freezing of homogeneous nucleated deliquesced hygroscopic aerosols is also accounted for, with the decrease in N_{wfa} represented by the second term on the RHS of Equation (5), while the freezing of existing water droplets is parameterized to be more effective in the presence of higher amounts of dust aerosols. Cloud ice sublimation returns the aerosols to N_{ifa} , the third term on the RHS of Equation (6).

In order to switch the ARI effects on, assumptions have to be made regarding the aerosol properties, in particular the single-scattering albedo, asymmetry factor and Angstrom exponent. Three aerosol models are available in WRF: rural, urban and maritime [64,65]. The rural aerosol model (ARI_R) is designed for cases where the contribution from urban and industrial sources is small. It assumes a mixture of 70% water soluble (ammonium, calcium sulphate, organic compounds) and 30% dust-like aerosols. The urban model (ARI_U) is a mixture of 80% rural aerosols and 20% carbonaceous or soot-like aerosols, which are assumed to have the same size distribution as both components of the rural model. As a result of the soot-like particles, the aerosols will be more absorbing [66]. The maritime aerosol model (ARI_M) also consists of two components: sea salt and a continental component assumed to be identical to the rural aerosol but with the very large particles removed, as they will eventually fall out as the air mass moves across water. Hence, the maritime aerosol model will be less absorbing than the default (rural) model. It is important to note that the assumptions made in the different aerosol models may not be in full agreement with the fraction of hygroscopic/non-hygroscopic aerosols at a given grid-point, which varies during the course of the model integration. Nevertheless, the three aerosol models are considered in this study to explore the sensitivity of the WRF predictions to the composition of the aerosol particles.

As an attempt to correct some of the model biases, different configurations of grid (or analysis) nudging [67,68] towards ERA-5 data are considered. They are discussed in Appendix A. In these runs, the horizontal wind components, water vapor mixing ratio and potential temperature perturbation are nudged on a timescale of 1 h above roughly 800 hPa, excluding the PBL. This nudging configuration is preferred so as to allow the model to develop its own structures while at the same time constraining the atmospheric circulation in the free atmosphere [69].

2.3. Observational and Reanalysis Datasets

In order to evaluate the best aerosol configuration for an increased model performance, two in situ and satellite-derived datasets are used. Station data collected by the National Center of Meteorology (NCM) is available at 30 automatic weather stations (AWS) and 5 airport stations, given in Figure 1. Air temperature, RH, sea-level pressure, and horizontal wind direction and speed are available every 15 min at the former and 1 h at the latter on 14 August 2013, with the downward shortwave radiation flux at the surface also measured at the location of the AWS. Daily accumulated precipitation is available for all 35 stations. In addition to the surface/near-surface measurements, the 00 and 12 UTC radiosonde profiles at Abu Dhabi’s International Airport (24.4331° N, 54.6511° E) from the National

Oceanic and Atmospheric Administration Integrated Radiosonde Archive (IGRA; [70,71]) are considered.

The satellite-derived datasets comprise (i) Red Green Blue (RGB) satellite images obtained from the Spinning Enhanced Visible and Infrared Imager (SEVIRI) instrument onboard the Meteosat Second Generation spacecraft [72], and (ii) Infrared Brightness Temperature (IRBT) maps from a combination of European, Japanese and United States geostationary satellites provided by the National Center for Environmental Prediction/Climate Prediction Center [73]. RGB images are available every 15 min on a 0.05° (~ 5.6 km) grid for the domain 60° S– 60° N and 60° W– 60° E on the European Organisation for the Exploitation of Meteorological Satellites (<https://eoportal.eumetsat.int/>, accessed on 22 June 2021) website. These images are processed to display relevant features such as dust, sand and clouds in contrasting colours following [72]. The IRBT maps are at 4 km spatial resolution and 30 min temporal resolution, available from 60° S– 60° N on the National Aeronautic and Space Administration's EarthData website (https://disc.gsfc.nasa.gov/datasets/GPM_MERGIR_1/summary, accessed on 6 May 2021).

Besides the listed observational datasets, the Modern-Era Retrospective analysis for Research and Applications version 2 (MERRA-2; [74]) data is also considered in this work. MERRA-2 explicitly accounts for aerosols and their interactions with the climate system, and is used to assess the spatial distribution of aerosols over the UAE on 14 August 2013 given the gaps and missing data in observation-derived products due to the extensive cloud cover. MERRA-2 provides aerosol-related variables such as the AOD on a $0.625^\circ \times 0.5^\circ$ global grid and on an hourly basis. It has been shown to perform well in the Arabian Peninsula when compared to satellite-derived and ground-based measurements [75,76], and is therefore suitable to be used here.

2.4. Verification Diagnostics

The performance of the WRF model is evaluated with the verification diagnostics proposed by [77]. In particular, the model bias, normalized bias (μ), correlation (ρ), variance similarity (η), and normalized error variance (α), defined in Equations (7)–(12) below, are employed.

$$\mathbf{D} = \mathbf{F} - \mathbf{O}, \quad (7)$$

$$BIAS = \langle \mathbf{D} \rangle = \langle \mathbf{F} \rangle - \langle \mathbf{O} \rangle, \quad (8)$$

$$\mu = \frac{\langle \mathbf{D} \rangle}{\sigma_{\mathbf{D}}}, \quad (9)$$

$$\rho = \frac{1}{\sigma_{\mathbf{O}}\sigma_{\mathbf{F}}} \langle (\mathbf{F} - \langle \mathbf{F} \rangle) \cdot (\mathbf{O} - \langle \mathbf{O} \rangle) \rangle, -1 \leq \rho \leq 1, \quad (10)$$

$$\eta = \frac{\sigma_{\mathbf{O}}\sigma_{\mathbf{F}}}{\frac{1}{2}(\sigma_{\mathbf{O}}^2 + \sigma_{\mathbf{F}}^2)}, 0 \leq \eta \leq 1, \quad (11)$$

$$\alpha = \frac{\sigma_{\mathbf{D}}^2}{\sigma_{\mathbf{O}}^2 + \sigma_{\mathbf{F}}^2} \equiv 1 - \rho\eta, 0 \leq \alpha \leq 2, \quad (12)$$

In the equations above, \mathbf{D} is the discrepancy between the model forecast \mathbf{F} and the observations \mathbf{O} , while $\langle \mathbf{X} \rangle$ and $\sigma_{\mathbf{X}}$ are the mean and standard deviation of \mathbf{X} , respectively.

The bias is defined as the mean discrepancy between the WRF predictions and the observations, $\langle \mathbf{D} \rangle$, while the normalized bias is the ratio of the bias to the standard deviation of the discrepancy, $\sigma_{\mathbf{D}}$. The latter is used to assess whether the model biases can be regarded as significant: as explained in [77], if $|\mu| < 0.5$, the contribution of the bias to the Root-Mean-Square-Error is less than roughly 10%, and hence the biases can be deemed as not significant. The correlation (ρ) and the normalized error variance (η) are a measure of the phase and amplitude agreement between the observed and modelled signals, respectively, with the two sources of error accounted for in the α diagnostic. For a random forecast based on the climatological mean, $\rho = 0$ and hence $\alpha = 1$. Hence, a model prediction is considered as practically useful if $\alpha < 1$. The ρ , η and α diagnostics are non-dimensional

quantities, symmetric with respect to the observations and forecasts, and applicable to both scalar and vector variables, making them suitable to be used in this work. Further details regarding the listed diagnostics can be found in [77].

3. Description of the Event (14 August 2013)

On 14 August 2013, deep convection and a dusty environment were ubiquitous in the UAE, as seen in Figure 3. The RGB and IRBT maps in the afternoon and evening hours, given in the first two rows, show a rapid flare-up of convection in the local early afternoon hours, which affected mostly the western and central parts of the country. The IRBT values dropped to around 190 K, indicating rather cold cloud tops, a sign of very deep convection [78], with the thick high-level clouds shaded in brown in the RGB images. Such low values of IRBT are more typical of tropical convective activity, such as that seen in tropical disturbances [79], than the average summertime convection in the UAE [31]. A second but less intense round of convection occurred in the evening to nighttime hours, with isolated convective cells developing over eastern UAE and western Oman in early to mid-afternoon hours, when convection typically flares up here [31].

Besides the unstable environment, on this day the atmosphere was also rather dusty. The third row of Figure 3 gives the AOD from MERRA-2 reanalysis data. Values in excess of two were seen over the western half of the UAE at 11 UTC (15 LT), decreasing during the afternoon and early evening hours. While these are not unusually high values for this region [40], AODs higher than two are commonly seen during dust storms [80]. Some of the reduction in the AOD may be attributed to transport by the low-level circulation, but the fact that the dusty region overlaps at least partially with the convection region suggests that convection–aerosol interactions have likely taken place.

The 14 August 2013 event was chosen by manually inspecting hourly IRBT and MERRA-2 AOD images for the summertime (June to September) periods for which NCM data were available, and selecting the one where the deepest convection, as given by the lowest IRBT, and the dustier environment, as given the highest AOD, co-occurred in the UAE.

Figures 4 and 5 show the sea-level pressure, 2 m water vapor mixing ratio, and low-level winds on 14 August 2013 from ERA-5 every 2 h from 08 UTC (12 LT) to 18 UTC (22 LT). The AHL is initially over the UAE and surrounding region, but at 12 UTC it shifts westward, lying over western parts of the country and extending into Saudi Arabia and Qatar, where the minimum sea-level pressure lies. The counterclockwise circulation around the AHL converges with the daytime sea-breeze from the Arabian Gulf and Sea of Oman. This convergence is more evident around 12–14 UTC (16–18 LT), Figure 4c,d, over central and western parts of the country, around the time when convection flared up rapidly (Figure 3a,b,d,e). The low-level convergence weakened after 16 UTC (20 LT), Figure 4e, when both the AHL and the sea-breeze faded away. The convective clouds that developed over eastern UAE were likely triggered by the convergence of the AHL circulation with the sea-breeze from the Sea of Oman and topographically driven flows (cf., Figure 4c,d and Figure 3d). Figure 5 shows that the near-surface air was rather moist over the country on this day, with water vapor mixing ratios typically in the range 15–20 g kg⁻¹. Together with the low-level wind convergence, the large-scale environment was suitable for the occurrence of deep convection. A comparison of the satellite images, Figure 4a,f, with the ITD drawn as a solid white line in the panels of Figure 5, reveals that, at least on this day, the clouds tended to develop around this convergence line. It is interesting to note that the ITD on this day reached southern parts of Iran to the north of the UAE, a behaviour that is expected in the warmer months. As explained in [35], the inland moistening by the sea-breezes from the Arabian Gulf, Sea of Oman and Arabian Sea allows the 15 °C isoline of dewpoint temperature, the metric used to diagnose the position of the ITD, to propagate northwards into the Arabian Gulf, as seen in Figure 5.

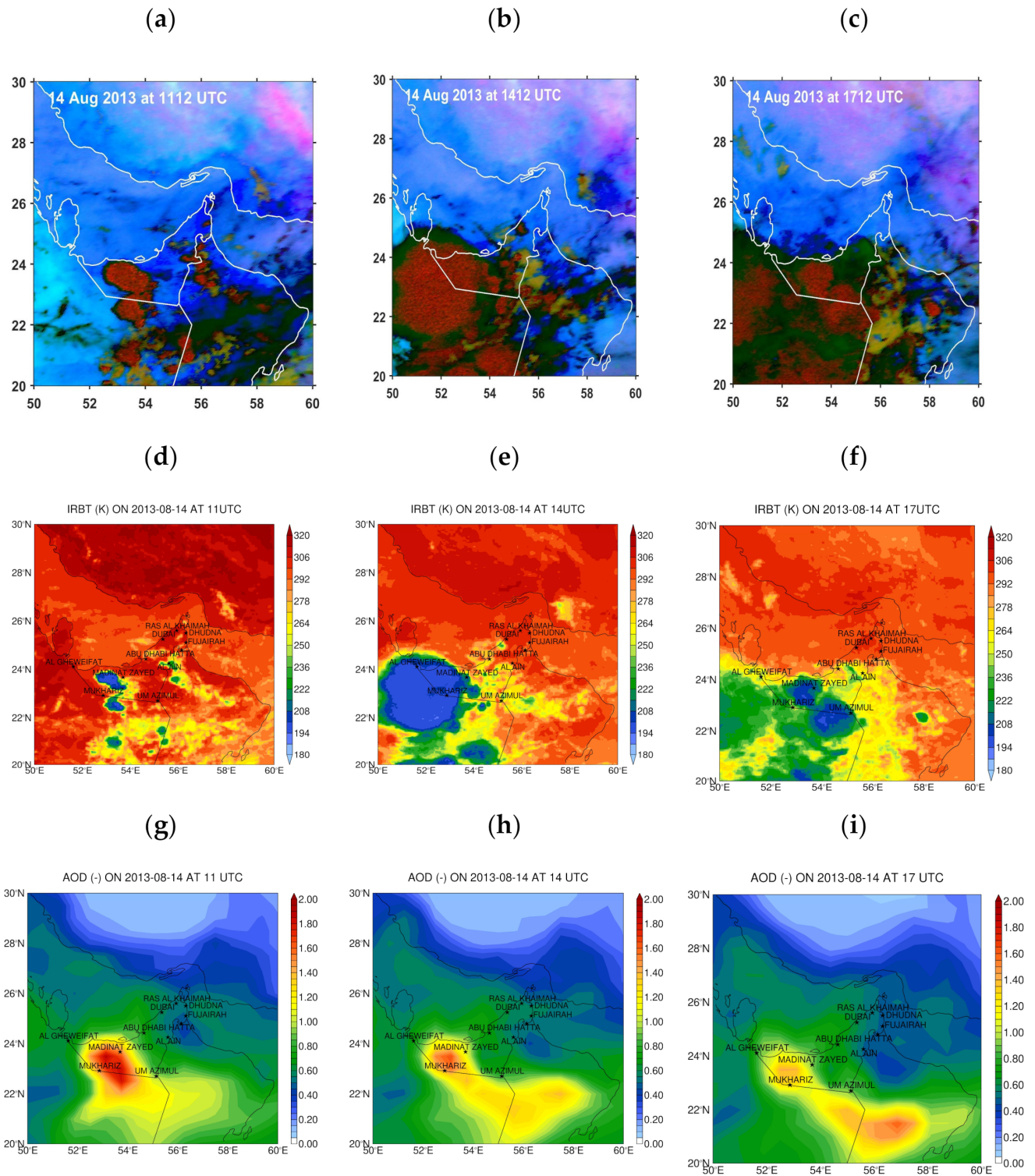


Figure 3. False-color RGB satellite images derived from the measurements taken by the SEVIRI instrument over the southern Arabian Peninsula on 14 August 2013 at around (a) 11 UTC, (b) 14 UTC and (c) 17 UTC. In the panels the magenta to pink shading denotes dust, while white regions are sandy areas. Thick high-level clouds are shaded in orange or brown, while thin high-level clouds are given in dark brown to black. Dry land is shaded in pale blue during daytime and pale green at night. (d–i) are as (a–c) but for the satellite-derived IRBT (K) and the AOD (non-dimensional) from MERRA-2 reanalysis, respectively.

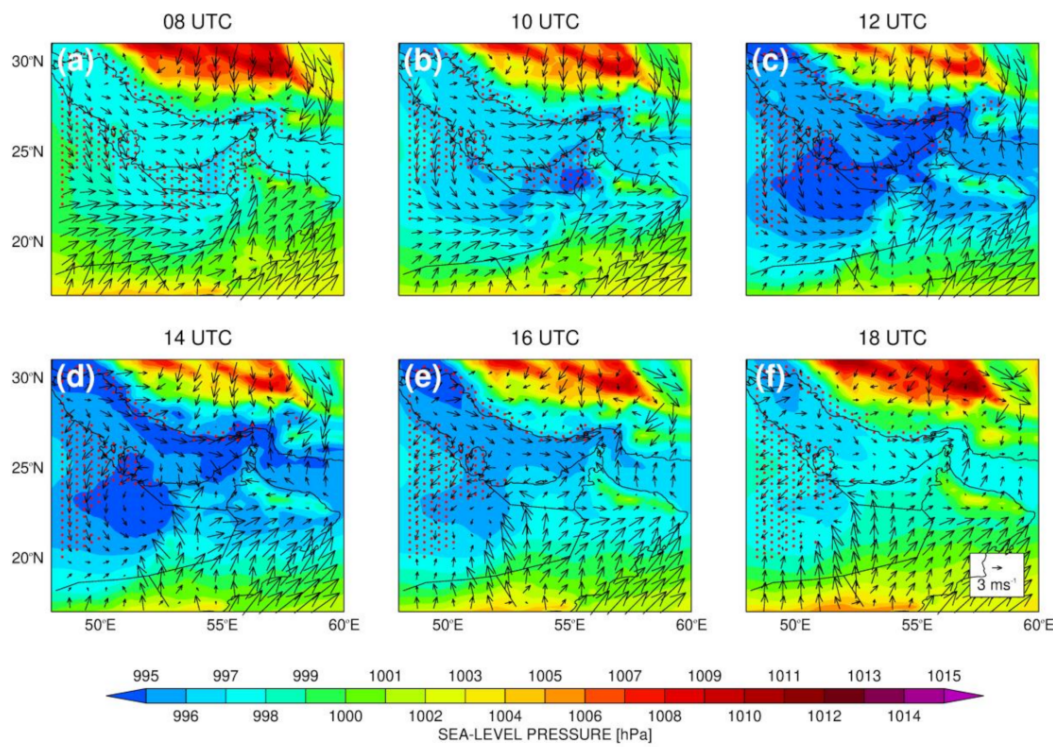


Figure 4. Sea-level pressure (shading; hPa) and 10 m horizontal wind vectors (arrows; m s^{-1}) at (a) 08 UTC, (b) 10 UTC, (c) 12 UTC, (d) 14 UTC, (e) 16 UTC and (f) 18 UTC on 14 August 2013 from ERA-5 data. The dotted region gives the AHL, defined based on the low-level (700–925 hPa) atmospheric thickness (m), following [35].

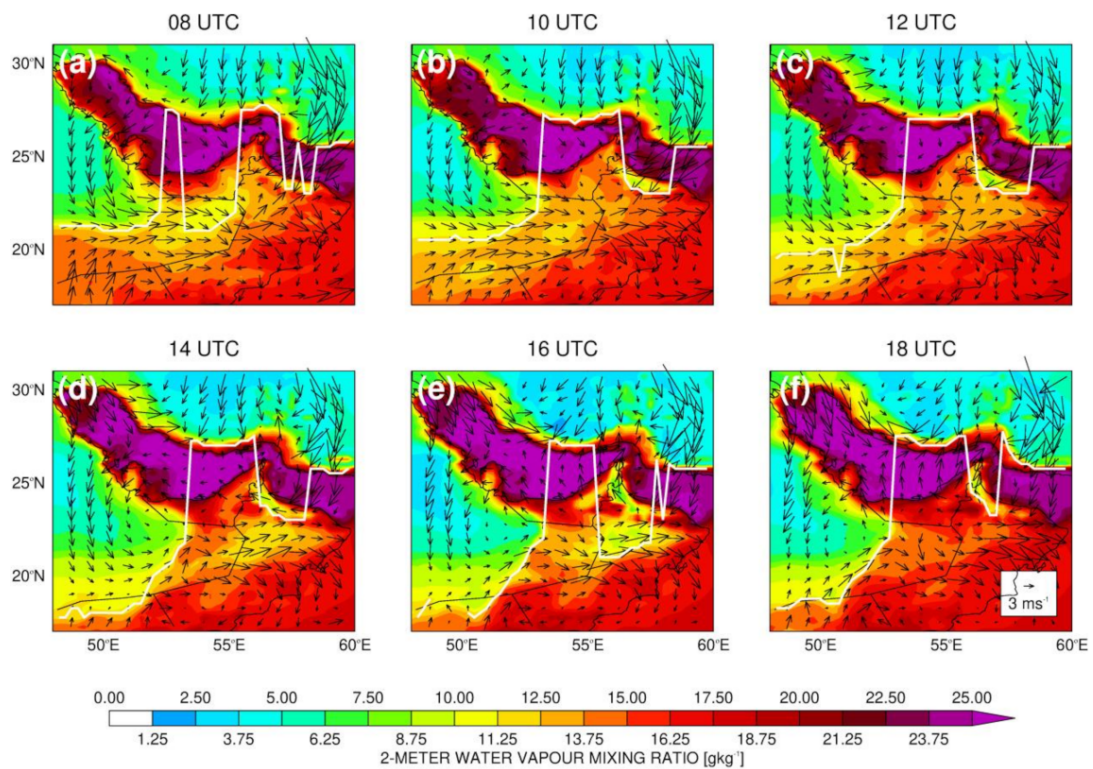


Figure 5. Sea-level pressure (shading; hPa) and 10 m horizontal wind vectors (arrows; m s^{-1}) at (a) 08 UTC, (b) 10 UTC, (c) 12 UTC, (d) 14 UTC, (e) 16 UTC and (f) 18 UTC on 14 August 2013 from ERA-5 data but for the 2 m water vapor mixing ratio (g kg^{-1}) in shading and the 850 hPa horizontal wind vector (m s^{-1}) in arrows. The solid white line gives the ITD defined using the 15°C isoline of dewpoint temperature (isodrosotherm).

A comparison of the AOD plots given in Figure 3g–i with the 10 m horizontal wind vectors plotted in Figure 4 indicates that the accumulation of aerosols over western UAE is related to the presence of a closed atmospheric circulation associated with the AHL in the region. The decreasing values of AOD in the evening to night time hours, are likely due to the advection of cleaner air from the south (cf., Figure 4e,f), as well as due to the washout and clearing of the air after the occurrence of precipitation. As far as the dust emission is concerned, two factors are at play: (i) dust lifted by strong near-surface winds triggered by cold pools and downbursts in association with the deep convection that developed on this day, a well-known mechanism for dust lifting in arid regions [81–83]; (ii) strong southerly winds in the early morning, from the combined effect of the AHL and sea–land breeze circulations, with the low-level wind convergence by high turbulent winds at the leading edge of the ITD [84,85] aiding in the dust-lifting activities (Figure 5a,b).

4. WRF Simulations

4.1. Aerosol Loading

Figure 6 shows the concentration of water- and ice-friendly aerosols in the lowest model layer for the simulations with the idealized (WRF-IDEAL) and the climatological (WRF-CLIM) aerosol distribution, the former multiplied by a factor of 10 so that the two have the same order of magnitude. The fact that the idealized profile is cleaner than the climatological profile is not surprising: as stated in Section 2.2, the idealized distribution was designed for the continental United States, where the atmosphere is cleaner compared to that in the UAE and surrounding region. In fact, over India and during the summer monsoon, the observed aerosol loading within the boundary layer, as measured at the surface and by aircrafts, was found to be roughly 10 times larger than that employed in the idealized profiles in WRF [86]. The spatially uniform aerosol loading at the start of the run in Figure 6a, in line with the way it is coded in the model, contrasts with a heterogeneous pattern in the simulation forced with the seven-year climatological aerosol loading. The higher amounts of water-friendly aerosols (sulphates, sea salt, organic matter) over the Arabian Gulf and of ice-friendly aerosols (mineral dust) over inland areas in Saudi Arabia and Oman are consistent with the fact that the former is typically advected from industrial and urban sites as well as from water bodies by the background northwesterly winds, while the latter has its main source in the Rub' Al Khali desert [40]. Despite differences in the initialization and order of magnitude, the spatial pattern of aerosol loading is similar in the two configurations, with a marked northwest–southeast gradient over the UAE. This can be explained by the near-surface circulation, given in Figure 7a for WRF-CLIM (similar results are obtained for WRF-IDEAL, not shown). A comparison with Figure 7b, same fields but from ERA-5, reveals that the AHL in WRF at 12 UTC, and as given by the sea-level pressure, is broader and displaced to the southeast with respect to that in ERA-5. The associated cyclonic circulation acts to slow down the progression of the sea-breeze over central and eastern parts of the country, where the model is drier than the reanalysis dataset, and speed it up over western UAE, where WRF is moister as the daytime sea-breeze is reinforced by the AHL circulation. This explains why, as shown in Figure 6, the higher aerosol concentrations over the Gulf extend well inland in the western half of the country, but are mostly confined to coastal areas elsewhere.

Figure 8 gives the vertically averaged profiles over the UAE at 00 and 12 UTC for both WRF-IDEAL and WRF-CLIM simulations. The decrease in aerosol concentration with height is more pronounced in the runs with the climatological profile, and in particular for the ice-friendly aerosols. This is consistent with the fact that dust is primarily present at low elevations as its source is surface emissions in semi-arid/arid regions [40], whereas other aerosol types have varied sources and are more ubiquitous in the troposphere. The diurnal variability is small except at low elevations, below 700 hPa, where the well-mixed daytime boundary layer leads to approximately constant values with height, whereas at night the concentrations are higher just above the surface, as the aerosols are trapped below the low-level nighttime surface-based inversion and in the residual mixed layer above it. This

variability is in line with the findings of [40,87]. The aerosol concentration profile shown in Figure 8 resembles the observed profiles measured during dedicated field campaigns [88].

An assessment of the WRF-predicted vertical aerosol profiles against those observed, which may feature multiple dust layers [87–89], as well as their composition and optical properties, is not possible due to the lack of observational data. An evaluation of the model-predicted AOD, which is a column integral and gives information on the attenuation of the incoming solar radiation as it goes through the atmosphere, against that estimated from ground-based and satellite assets, also cannot be conducted due to the extensive cloud cover on this day (Figure 3a–c) and the resulting gaps and missing data in the observed estimates (not shown). However, the WRF-predicted AOD can be compared with that of MERRA-2 reanalysis data, as shown in Figure 9. The WRF-5×CLIM-ARI_R-NUDGE simulation, for which the climatological aerosol distribution is multiplied by a factor of 5, gives the best agreement with the MERRA-2 AOD out of all model configurations considered. However, even in this simulation the atmosphere in WRF is slightly dustier, in particular in the afternoon hours, likely due to a lack of precipitation that precludes a washout of the aerosols and a cleaning of the air, as discussed in the next section. In any case, and even though MERRA-2 is taken as a reference for this comparison, it is important to note that, despite the data assimilation, this dataset still has biases when compared to observed measurements, mostly due to missing emissions and/or deficiencies in the parameterization schemes, as noted in [90]. The lack of ground-based measurements on this day, however, precludes an evaluation of the quality of the MERRA-2 forecasts over the UAE.

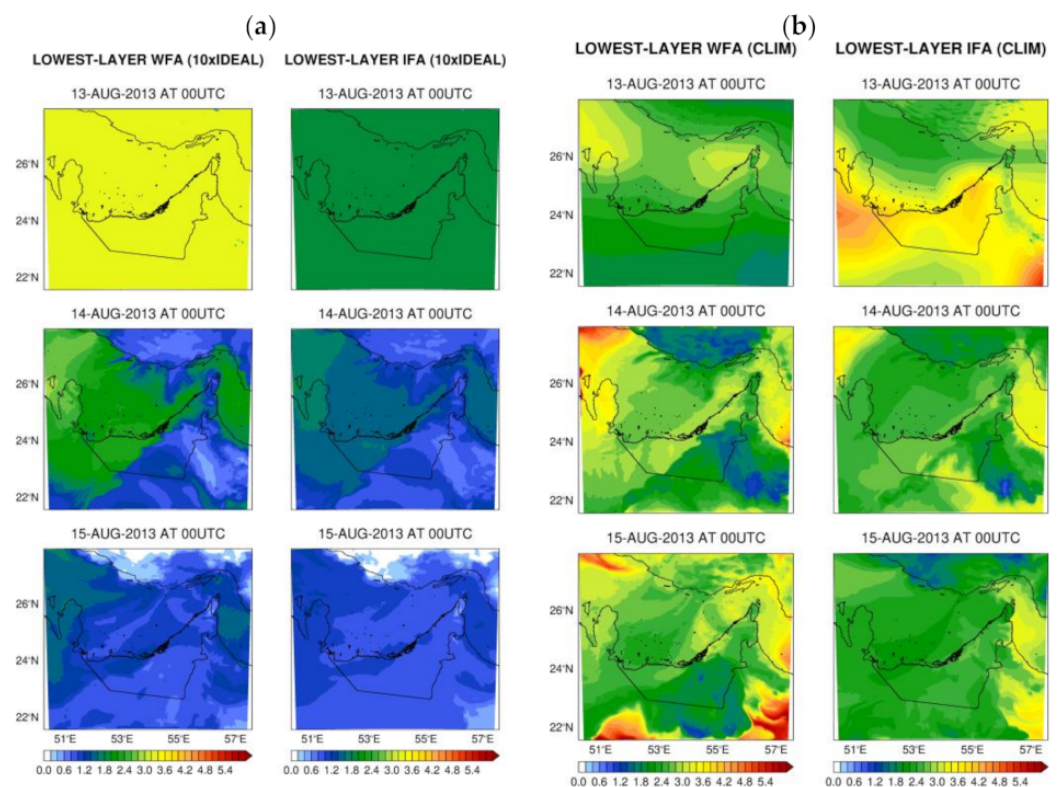


Figure 6. Concentration (number kg^{-1}) of water- (10^9 number kg^{-1}) and ice-friendly (10^7 number kg^{-1}) aerosols in lowest WRF layer at the start of the run (13 August at 00 UTC) and after 24 h (14 August at 00 UTC) and 48 h (15 August at 00 UTC) for the (a) WRF-IDEAL (with the aerosol amounts multiplied by a factor of 10 for easiness of comparison with the climatological distribution) and (b) WRF-CLIM simulations. The fields are shown for the innermost (2.5 km) WRF grid.

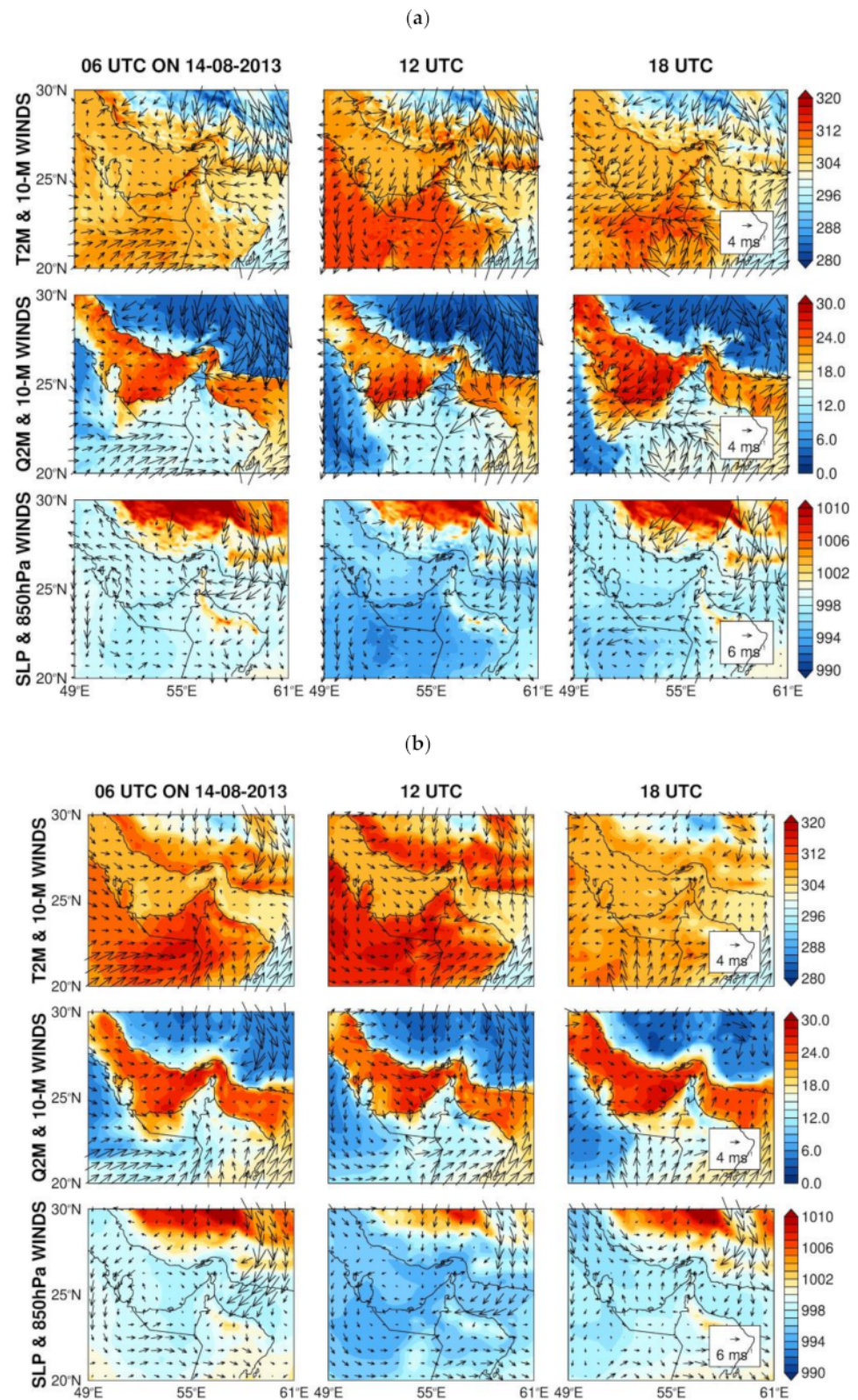


Figure 7. The 2 m air temperature (K) and 10 m wind vector (m s^{-1}) (top row), 2 m water vapor mixing ratio (g kg^{-1}) and 10 m wind vector (m s^{-1}) (middle row), and sea-level pressure (hPa) and 850 hPa wind vector (m s^{-1}) (bottom row) on 14 August 2013 at 06, 12 and 18 UTC from the (a) 7.5 km grid of the WRF-CLIM simulation and (b) ERA-5 reanalysis data.

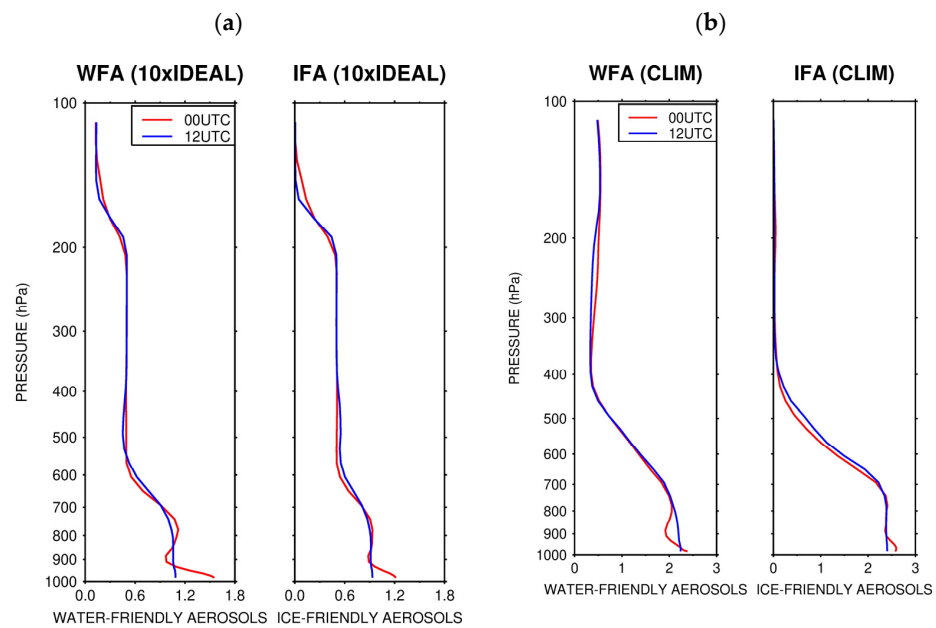


Figure 8. UAE-averaged vertical profiles of the water-friendly (left; 10^9 number kg^{-1}) and ice-friendly (right; 10^7 number kg^{-1}) aerosol concentration at 00 UTC (red) and 12 UTC (blue) on 14 August 2013 for the 2.5 km grid of the (a) WRF-IDEAL (with the aerosol amounts multiplied by a factor of 10 for easiness of comparison with the climatological distribution) and (b) WRF-CLIM simulations.

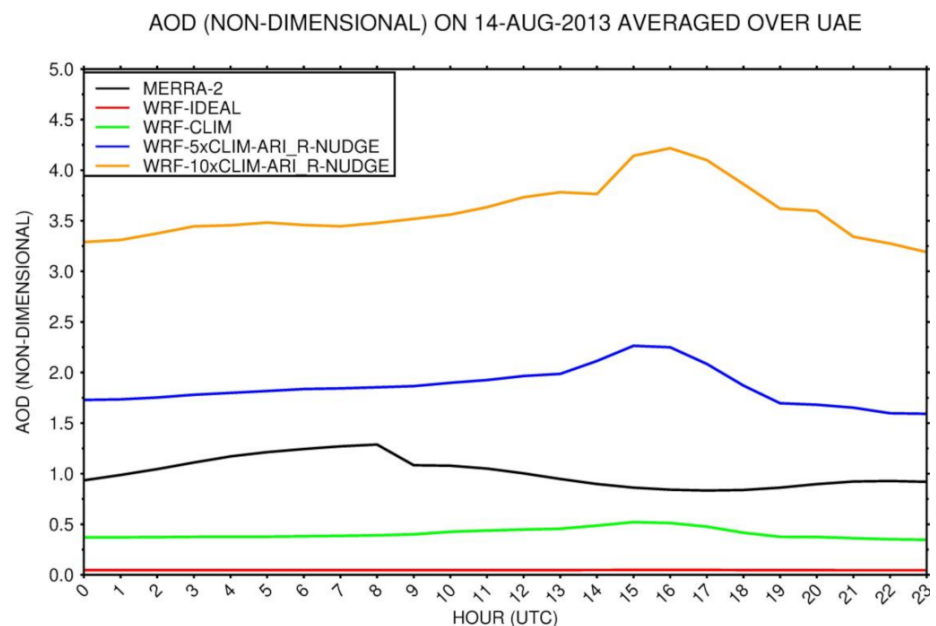


Figure 9. UAE-averaged AOD from MERRA-2 (black) and from the 2.5 km grid of the WRF-IDEAL (red), WRF-CLIM (green), WRF-5×CLIM-ARI_R-NUDGE (blue) and WRF-10×CLIM-ARI_R-NUDGE (orange) simulations for 14 August 2013.

4.2. Aerosol Interaction with Convection

4.2.1. ARI on Idealized and Climatological Aerosol Distributions

In order to investigate the impact of switching on the ARI on the simulations with the idealized and climatological aerosol distributions, Figure 10 shows the WRF bias, with respect to the hourly station data, for air temperature, water vapor mixing ratio, horizontal wind speed and surface downward shortwave radiation flux, averaged over all 35 NCM stations on 14 August 2013. The scores averaged over all hours of the day are given in Table 3.

As expected, when the ARI is switched on there is a decrease in the shortwave radiation flux reaching the surface (Figure 10d), which is more pronounced for the run with the climatological distribution owing to the higher aerosol loading. Compared to the simulations where it is switched off, the maximum reduction in the radiation flux is $\sim 10 \text{ W m}^{-2}$ for the run with the idealized aerosol distribution and $\sim 40 \text{ W m}^{-2}$ for the run with the climatological aerosol distribution, with daily averaged values of 3 W m^{-2} and 20 W m^{-2} , respectively. Despite the small decrease in the downward shortwave radiation flux, however, WRF continues to largely overestimate the observed values, which can be attributed to a lack of clouds in the model, a bias that has been noted by several authors [48,91,92]. Given the lack of clouds, the ARI effects will prevail over the ACI effects, and hence the model predictions for simulations WRF-IDEAL, WRF-IDEAL-ARI_R, WRF-CLIM and WRF-CLIM-ARI_R will be comparable, as the radiative impacts of switching on the ARI are small. This can be seen in fields such as the air and surface temperatures, for which the decreases are within 0.5 K and 1 K, respectively, when the ARI effects are activated. These changes are comparable to those reported by other authors for a similar variation in the surface radiation fluxes [22,93].

In all simulations, WRF is much colder than observations, with biases of up to 7 K and a daily average around 2.5 K. This has been reported in the literature [46,48], with the discrepancy more pronounced in the warmer months and not being restricted to the Arabian Desert [94]. It may arise from deficiencies in the physical parameterization schemes, in particular in the LSM and radiation schemes, and/or an incorrect representation of the atmospheric composition. Several attempts have been made to correct for this bias, such as employing different model configurations [34,95] and input data [19], tuning hard-coded parameters [46,96], and using more realistic lower boundary conditions [48]. The sensitivity experiments described in Figure 10 suggest that having a more realistic representation of the aerosol loading does not alleviate the cold bias either, with differences within $\pm 0.15 \text{ K}$ for the daily averaged air temperature (Table 3). It is then possible that the referred cold bias could be down due to a non-linear interaction of different model errors.

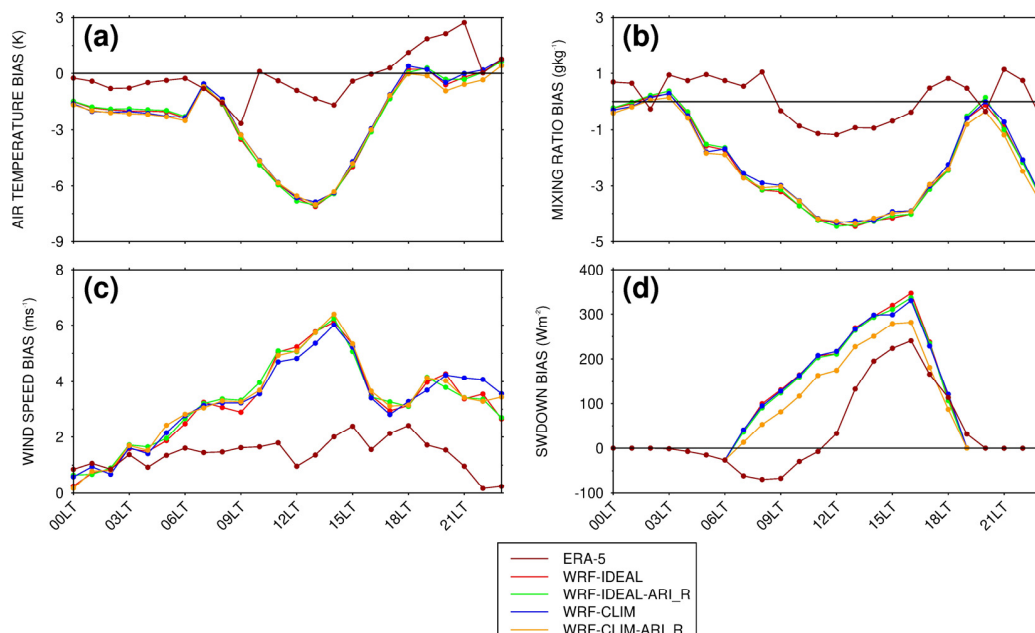


Figure 10. (a) The 2 m temperature ($^{\circ}\text{C}$), (b) 2 m water vapor mixing ratio (g kg^{-1}), (c) 10 m horizontal wind speed (m s^{-1}) and (d) surface downward shortwave radiation flux (W m^{-2}) bias with respect to the in situ measurements averaged over the location of the 35 NCM stations given in Figure 1, for the simulations WRF-IDEAL (red), WRF-IDEAL-ARI_R (green), WRF-CLIM (blue) and WRF-CLIM-ARI_R (orange). The brown line gives the biases for ERA-5. For both WRF and ERA-5, the values used for analysis are those at the closest grid-points to the location of the stations. The time in the horizontal axis is local time (LT; UTC+4) on 14 August 2013.

Table 3. Skill scores for air temperature, water vapor mixing ratio, sea-level pressure, downward shortwave radiation flux, horizontal wind vector and precipitation for all 35 NCM stations for the WRF simulations conducted in this study: WRF-IDEAL (WRF-1), WRF-IDEAL-ARI_R (WRF-2), WRF-CLIM (WRF-3), WRF-CLIM-ARI_R (WRF-4), WRF-CLIM-ARI_R-NUDGE (WRF-5), WRF-5×CLIM-ARI_R-NUDGE (WRF-6), WRF-5×CLIM-ARI_U-NUDGE (WRF-7), WRF-5×CLIM-ARI_M-NUDGE (WRF-8) and WRF-10×CLIM-ARI_R-NUDGE (WRF-9).

Field	Diagnostic	WRF-1	WRF-2	WRF-3	WRF-4	WRF-5	WRF-6	WRF-7	WRF-8	WRF-9
Temperature	BIAS (K)	−2.4720	−2.4530	−2.4050	−2.5551	−2.5464	−2.7312	−3.4674	−2.8168	−3.0556
	μ	−0.5263	−0.5219	−0.5166	−0.5603	−0.5746	−0.6649	−1.0292	−0.6428	−0.7843
	ρ	0.4113	0.4118	0.4255	0.4374	0.4655	0.5213	0.6299	0.4815	0.5504
	η	0.9979	0.9977	0.9975	0.9986	0.9989	1.0000	0.9859	0.9997	0.9993
	α	0.5896	0.5892	0.5756	0.5632	0.5350	0.4787	0.3790	0.5187	0.4499
Mixing Ratio	BIAS (g kg ^{−1})	−2.2123	−2.0726	−2.4731	−2.3181	−2.8098	−2.6691	−2.6477	−2.8422	−2.7686
	μ	−0.3835	−0.3605	−0.4279	−0.4004	−0.4713	−0.4315	−0.4205	−0.4603	−0.4170
	ρ	0.3511	0.3563	0.3565	0.3399	0.3942	0.3417	0.3341	0.3609	0.3041
	η	0.9915	0.9916	0.9933	0.9898	0.9999	1.0000	0.9995	0.9995	0.9962
	α	0.6519	0.6468	0.6459	0.6635	0.6059	0.6584	0.6661	0.6393	0.6970
SLP	BIAS (hPa)	3.0872	3.0702	3.0680	3.0084	2.7449	2.7320	2.6919	2.9786	2.8215
	μ	0.6995	0.6957	0.6940	0.6788	0.6292	0.6231	0.6210	0.6823	0.6438
	ρ	−0.0456	−0.0430	−0.0442	−0.0475	−0.0610	−0.0734	−0.0731	−0.0809	−0.0823
	η	0.8324	0.8318	0.8310	0.8303	0.8431	0.8431	0.8499	0.8474	0.8454
	α	1.0380	1.0358	1.0367	1.0394	1.0515	1.0619	1.0621	1.0686	1.0696
SWDOWN	BIAS (W m ^{−2})	99.4563	96.7037	97.7780	77.5172	73.7791	9.2294	−112.3040	35.3777	−45.8454
	μ	0.5863	0.5732	0.5717	0.4975	0.4742	0.0747	−0.5850	0.2613	−0.3298
	ρ	0.9082	0.9077	0.9059	0.9114	0.9111	0.9182	0.8415	0.9118	0.9077
	η	0.9736	0.9747	0.9738	0.9835	0.9838	0.9995	0.8341	0.9982	0.9595
	α	0.1175	0.1152	0.1178	0.1036	0.1036	0.0823	0.2981	0.0898	0.1291
Horizontal Wind	BIAS (SPEED; m s ^{−1})	3.0946	3.1309	3.1145	3.1785	3.5708	4.1674	3.1660	4.0691	4.4585
	μ (SPEED)	0.7686	0.7572	0.7667	0.7572	0.7817	0.8530	0.6813	0.8714	0.9156
	ρ	0.1557	0.1571	0.1407	0.1226	0.1293	0.0513	0.0785	0.0597	0.0182
	η	0.9728	0.9679	0.9717	0.9715	0.9568	0.9498	0.9252	0.9618	0.9545
	α	0.8485	0.8479	0.8633	0.8809	0.8763	0.9513	0.9274	0.9425	0.9826
PRECIPIATION BIAS (mm)	−42.4447	−40.5812	−51.0678	−50.4518	−38.0378	−41.5867	−35.7302	−48.5239	−45.6105	

Besides the cold temperatures (Figure 10a), the near-surface wind speed is also too strong when compared to that observed (Figure 10c). The two biases can be related, as too strong turbulent mixing will lead to cooler and drier near-surface conditions [97], the latter consistent with the negative mixing ratio biases of up to $−4.5 \text{ g kg}^{-1}$ (Figure 10b) and a daily average around $−2.2 \text{ g kg}^{-1}$ (Table 3). The stronger near-surface winds in the model are likely a result of an incorrect representation of its subgrid-scale fluctuations and deficiencies in the surface drag parameterization, as optimizing relevant parameters such as the roughness length does not seem to alleviate the problem [96]. Changing the aerosol loading by an order of magnitude only leads to differences of up to $\pm 0.2 \text{ m s}^{-1}$ in the daily mean wind speed (Table 3), or less than 6% of the daily averaged values. In a nutshell, the major impact of switching on the ARI is a decrease in the downward shortwave radiation flux, which reaches up to 40 W m^{-2} when the more opaque climatological distribution is employed. It is interesting to note that, for all fields given in Figure 10, the magnitude of the WRF biases exceed that of the response to changes in the aerosol loading and activation of the ARI.

The verification diagnostics when all hours of the day and 35 weather stations are considered are given in Table 3. In line with Figure 10, the scores are roughly comparable for the four simulations. Except for sea-level pressure, the α scores are always less than 1, indicating that the model predictions can be regarded as skilful. For all variables shown, phase errors dominate over magnitude errors, as η is typically larger than 0.95, while ρ is, at times, negative. A similar conclusion was reached by [92], in the analysis of cold season and warm season convective events in the UAE. The lack of clouds and the drier environment in the model will impact the diurnal cycle of variables such as air temperature and mixing ratio, which exhibit higher α values when compared to the shortwave radiation flux, for which the diurnal variability is rather well captured by WRF, with both ρ and η in excess of 0.9. The poorer scores for sea-level pressure are consistent with the incorrect simulation of the AHL (cf., Figure 7a,b), both in terms of its magnitude and temporal variability. On the other hand, the lower values of ρ (and hence higher values of α) for the wind vector are a reflection of its higher temporal and spatial variability, which are rather difficult to model in the UAE, as noted by [92,96]. Except for the water vapor mixing ratio, the absolute value of the normalized bias is generally higher than 0.5 for the four WRF simulations, meaning that the WRF tendency to under-predict the air temperature and overestimate the strength of the near-surface wind can be regarded as significant. Figure 11 shows the bias in the temperature and RH profiles at the location of Abu Dhabi's airport with respect to radiosonde data at 00 and 12 UTC on this day. In order to extract this quantity, first the observed and model-predicted data are interpolated in log-pressure coordinates to a pre-defined set of pressure levels from 1000 to 100 hPa at which the observational data is typically available, before the difference between each set of WRF and observed profiles is taken. The WRF temperature biases are typically within ± 2 K, having the largest amplitudes between 950 and 800 hPa at 00 UTC. The magnitude of the biases decreases from a peak of about 3 K for WRF-IDEAL-ARI_R to 1.5 K for WRF-CLIM-ARIR_R, with the warming consistent with the increased dust loading (Figures 8 and 9). A smaller warming tendency of up to 0.5 K is also seen when the ARI effects are switched on, in particular when the climatological aerosol loading is used (WRF-CLIM vs. WRF-CLIM-ARI_R). The temperature biases at 12 UTC have a reduced magnitude likely because of the well mixed vertical profile in the lower layers, which leads to a roughly uniform aerosol loading below 700 hPa (Figure 8). The RH vertical profile in WRF is much drier than in observations, in particular at 12 UTC, in line with the less moist near-surface environment. The tendency of the model to generate drier conditions at the site in the summer season was reported by [48] over the UAE and [98] over Qatar. Besides deficiencies in the physics schemes, the drier environment can be explained by a lack of clouds in WRF which is consistent with the reduced amounts of precipitation generated by the model (Table 3) and the cooler temperature profile (cf., Figure 11a), and has been found to be the case in summertime convective events in the region [19]. As an attempt to correct for the aforementioned model biases, different configurations of grid nudging were tested as discussed in Appendix A. In the subsequent model simulations, grid nudging is employed in the two outermost nests, as by and large it helps to improve the model performance (cf., WRF-CLIM-ARI_R with WRF-CLIM-ARI_R-NUDGE scores in Table 3).

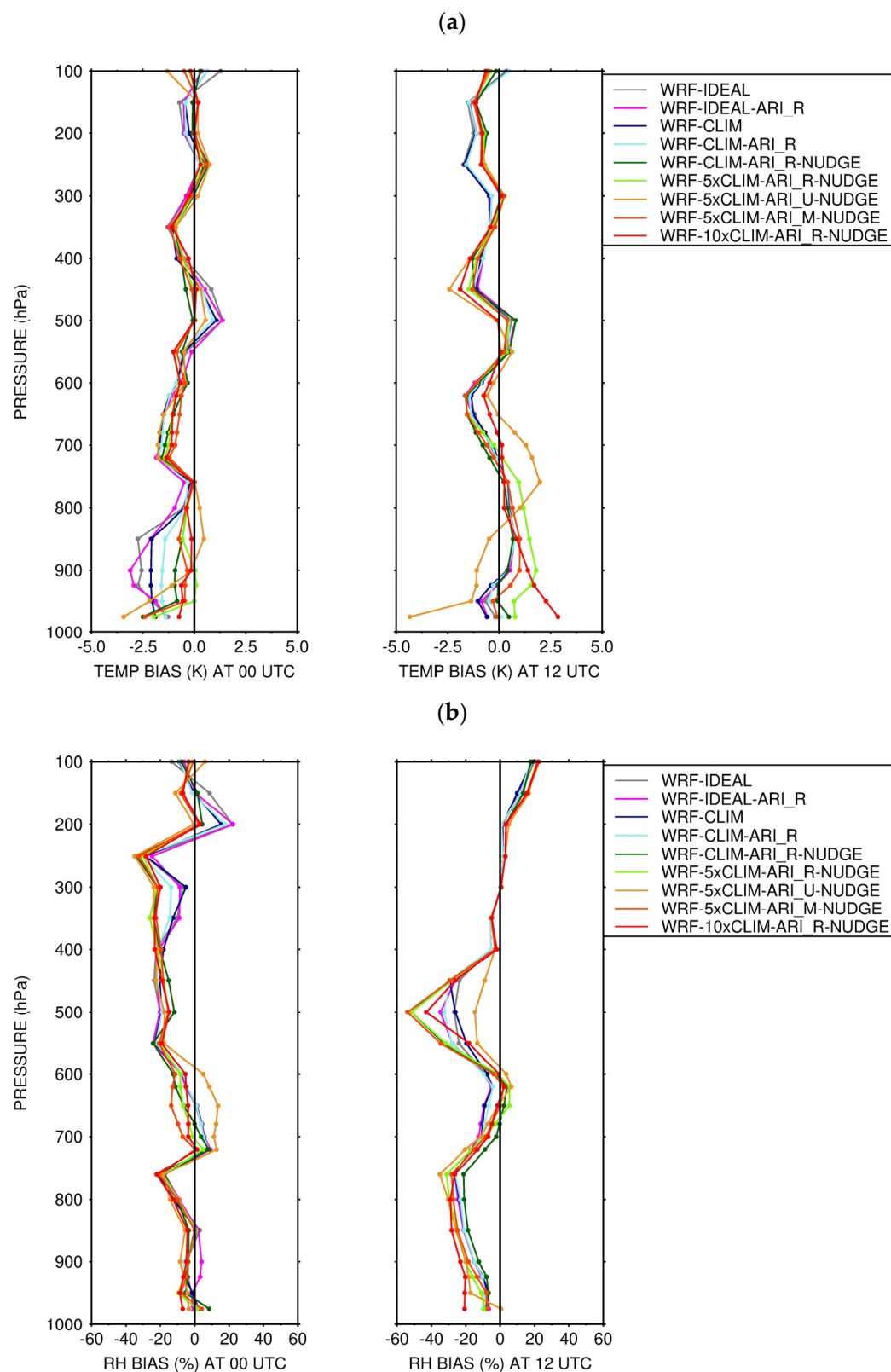


Figure 11. Bias of the WRF vertical profiles of (a) temperature (K) and (b) relative humidity (%) with respect to the radiosonde profiles launched at Abu Dhabi's airport on 14 August 2013 at 00 and 12 UTC for all nine simulations. The solid black vertical line in all panels gives the optimal score (i.e., zero bias).

On this day, the sum of the observed precipitation at all stations was 56.20 mm, most of which fell over southern parts of the country (Figure 12a). However, the model biases for runs WRF-IDEAL, WRF-IDEAL-ARI_R, WRF-CLIM and WRF-CLIM-ARI_R ranged between -42 and -51 mm, as shown in Table 3, indicating that less than a quarter of the observed precipitation is captured by WRF. As seen in Figures 12a–e and 13a–e, most of the rain and clouds in the model develop to the south of the UAE, due to a southward shift in the region of low-level wind convergence, as a result of a broader and stronger AHL. This shift can be seen by comparing Figure 7a,b, e.g., at 12 and 18 UTC, in ERA-5 the low-level convergence is mostly over central UAE, while in WRF it is further south and takes place later in the day, as the southerlies are weaker due to a more extensive thermal low. It is interesting to note that using the climatological aerosol loading leads to slightly drier conditions at the location of the NCM stations of 10–11 mm (Table 3), even though over the whole domain it rains more (Figure 12a–e) due to enhanced convection over northeastern Saudi Arabia (Figure 13a–e). The reduction in precipitation over the UAE in WRF-CLIM and WRF-CLIM-ARI_R compared to WRF-IDEAL and WRF-IDEAL-ARI_R may be attributed to the drier conditions (Table 3), as well as to the stabilizing effect aerosols have on the environment, with a heating of the aerosol layer and a cooling of the surface below [99]. However, aerosol precipitation effects are known to be highly sensitive to aerosol properties [100]. The drier environment in WRF-CLIM and WRF-CLIM-ARI_R is mostly over western UAE, where there is additional precipitation in WRF-IDEAL and WRF-IDEAL-ARI_R (Figure 12b–e) and is due to a late arrival of the sea-breeze that arises from a southeasterly shift in the position of the AHL (not shown). The changes in the position and strength of the AHL with the aerosol loading is discussed in more detail in Section 4.2.2. Over the whole domain, however, WRF-CLIM-ARI_R is wetter than WRF-IDEAL, WRF-IDEAL-ARI_R and WRF-CLIM. In fact, while at the location of the weather stations the impact of switching on the ARI on the model-predicted precipitation is rather small, generally less than 1 mm (Table 3), when the climatological distribution is used it leads to a $\sim 47\%$ increase in the domain-wise rainfall (Figure 12d,e). This arises from deeper convection, as shown by the colder cloud tops in Figure 13d,e as opposed to Figure 13b,c, with the stronger updrafts (Figure 14) leading to a higher fraction of aerosols being activated [49]. Figure 14 shows the maximum vertical velocity in the column, and the pressure level at which it is predicted, for runs WRF-CLIM and WRF-CLIM-ARI_R. In the latter the vertical velocity has a larger magnitude (56 m s^{-1} vs. 31 m s^{-1}), peaking in both at about 160 hPa, a sign of overshooting convection [101]. These findings are in line with the results of [17], who found that switching on the ARI effects delays the onset of convection due to the dust-stabilizing effects, but leads to more active cells later in the day, with an overall increase in rainfall.

The results in Figures 10, 12 and 13 and Table 3 indicate the model has biases in the simulation of the meteorological conditions on this day. As noted before, changes in the model physics and even the use of interior nudging in the outer grids failed to correct the major biases such as the surface cold bias, excessive downward shortwave radiation and stronger wind speeds. Despite this, however, the current WRF set up can be used to explore the sensitivity of the model forecasts to the aerosol loading and aerosol optical properties, which is the purpose of this study. This is carried out in Sections 4.2.2 and 4.2.3, respectively.

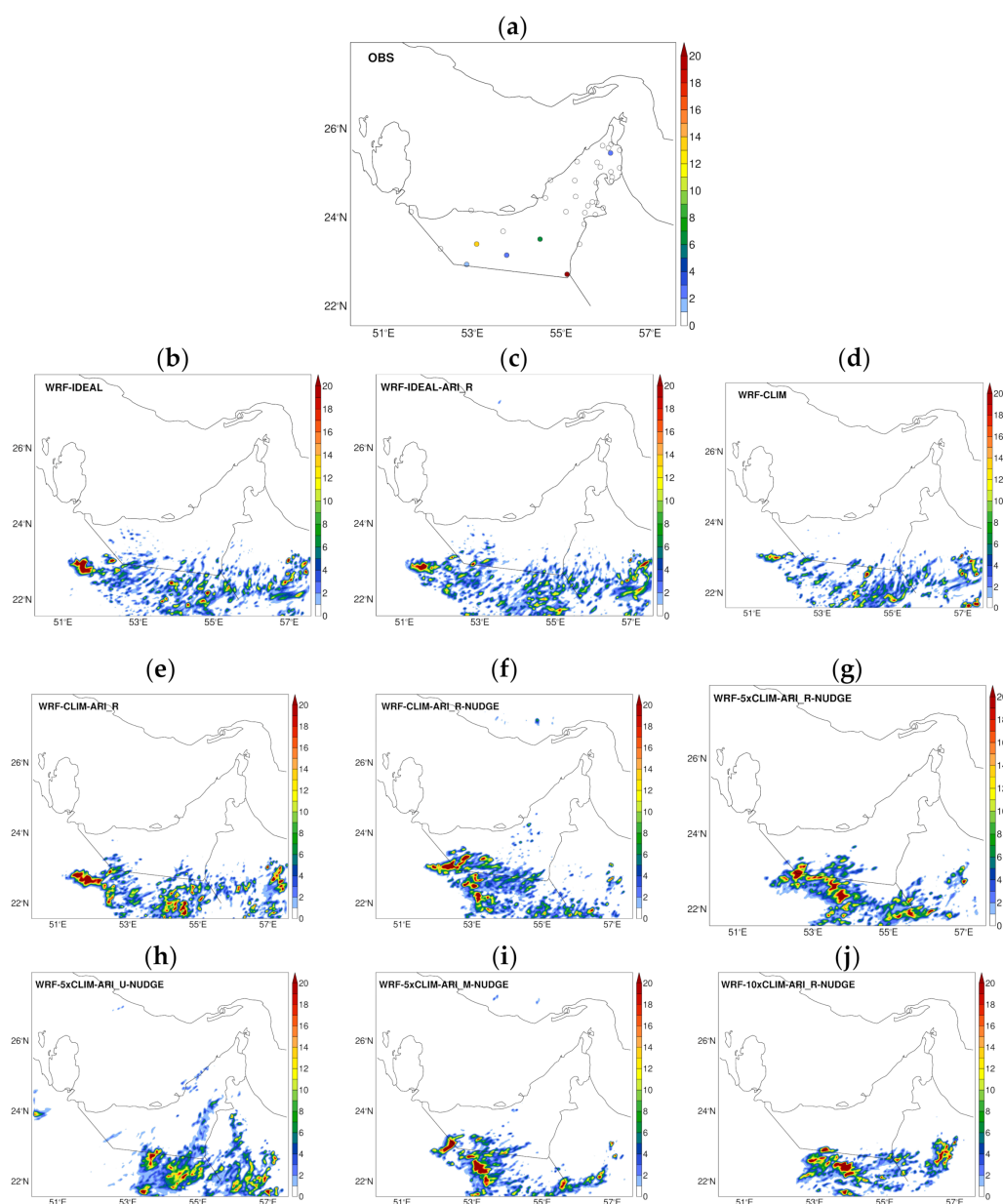


Figure 12. Total accumulated precipitation (mm) on 14 August 2013 (a) at the location of the 35 weather stations given in Figure 1 and (b–j) for the 2.5 km grid of all nine WRF simulations.

4.2.2. Sensitivity to Linear Scaling of Aerosol Loading

In this subsection, the impact of the aerosol loading on the WRF predictions of convection over the UAE is analysed. Figure 15 shows the surface upward and downward shortwave and longwave radiation fluxes averaged over the whole of the UAE for all hours of the day on 14 August 2013, for simulations WRF-CLIM-ARI_R-NUDGE, WRF-5×CLIM-ARI_R-NUDGE and WRF-10×CLIM-ARI_R-NUDGE. The downward shortwave radiation flux at the surface decreases in a roughly linear fashion as the aerosol loading is increased, with a drop of up to 180 W m^{-2} for WRF-5×CLIM-ARI_R-NUDGE and 360 W m^{-2} for WRF-10×CLIM-ARI_R-NUDGE with respect to WRF-CLIM-ARI_R-NUDGE, while the upward shortwave radiation flux is cut by up to 40 W m^{-2} and 81 W m^{-2} for the same simulations, respectively. In a daily average sense, and with respect to WRF-CLIM-ARI_R-NUDGE, the net shortwave radiation flux decreases by 46 W m^{-2} in WRF-5×CLIM-ARI_R-NUDGE and 91 W m^{-2} in WRF-10×CLIM-ARI_R-NUDGE. Assuming a linear scaling, for a doubling of the aerosol amount the change in the net shortwave radiation flux would be

about -18 W m^{-2} , in line with the values reported by [22] for a study over West Africa. On the other hand, the impact on the longwave radiation flux is much smaller, with hourly changes in the net flux of up $+62 \text{ W m}^{-2}$ and $+129 \text{ W m}^{-2}$ for runs WRF-5 \times CLIM-ARI_R-NUDGE and WRF-10 \times CLIM-ARI_R-NUDGE with respect to WRF-CLIM-ARI_R-NUDGE, and daily averaged values of $+25 \text{ W m}^{-2}$ and $+51 \text{ W m}^{-2}$, respectively. These changes are smaller by a factor of two than those estimated by [22]. This may be explained by the aerosol properties used in the model, which the longwave radiative forcing is known to be highly sensitive to [102,103]. As seen in Figure 15b, the downward longwave radiation flux exhibits a change of less than $\pm 10 \text{ W m}^{-2}$, as this field is mostly a function of the atmospheric emissivity and cloud cover, both of which vary less than the surface temperature [104]. The upward longwave radiation flux, on the other hand, is lower for higher aerosol loadings as the surface temperature drops, but the maximum reduction is still less than a factor of two to three smaller than the decrease in the downward shortwave radiation flux. This is because the temperature does not vary much in absolute values, as it is estimated from the surface energy budget, with the different terms adjusting to a varying downward shortwave radiation flux [55]. As for the shortwave radiation flux, the changes in the surface longwave radiation fluxes scale roughly linearly with the aerosol loading, in line with the findings of [105] for a field campaign in the Cape Verde islands in September 2006.

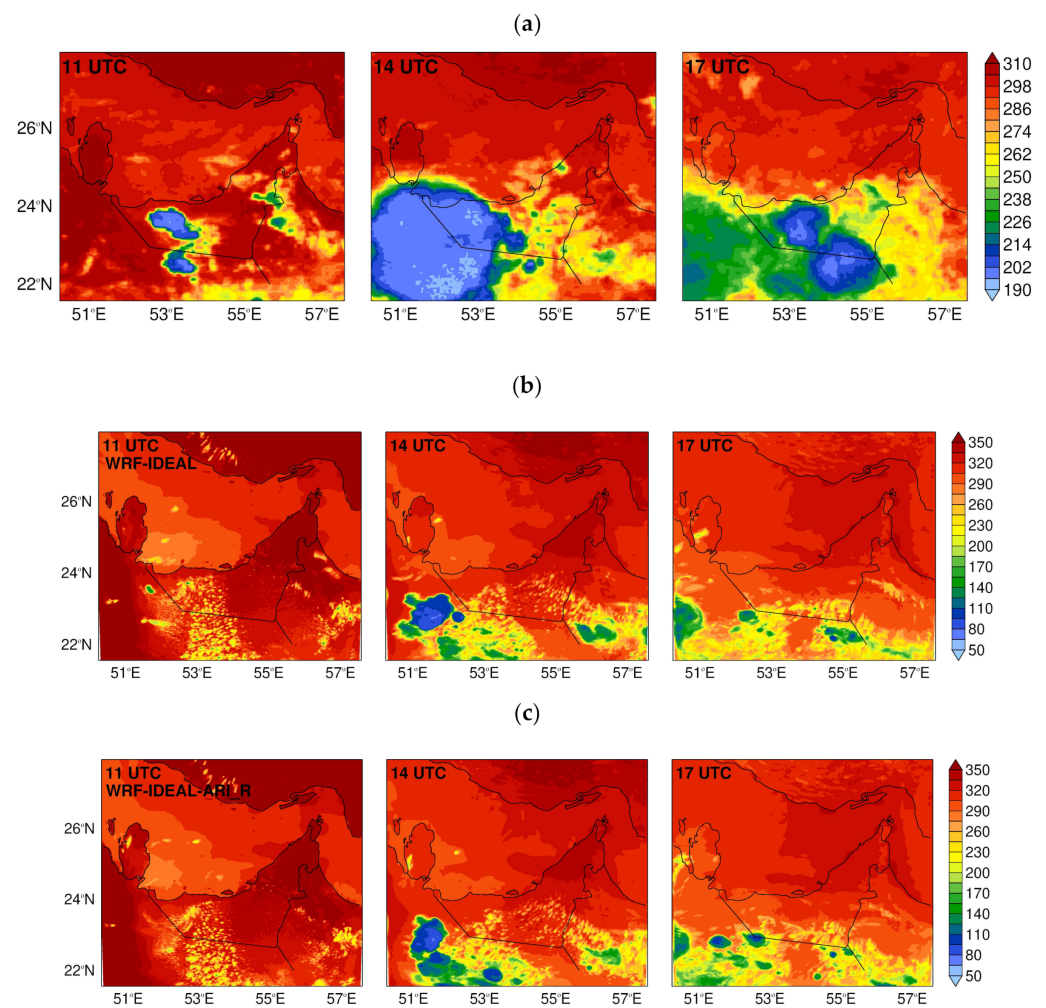


Figure 13. Cont.

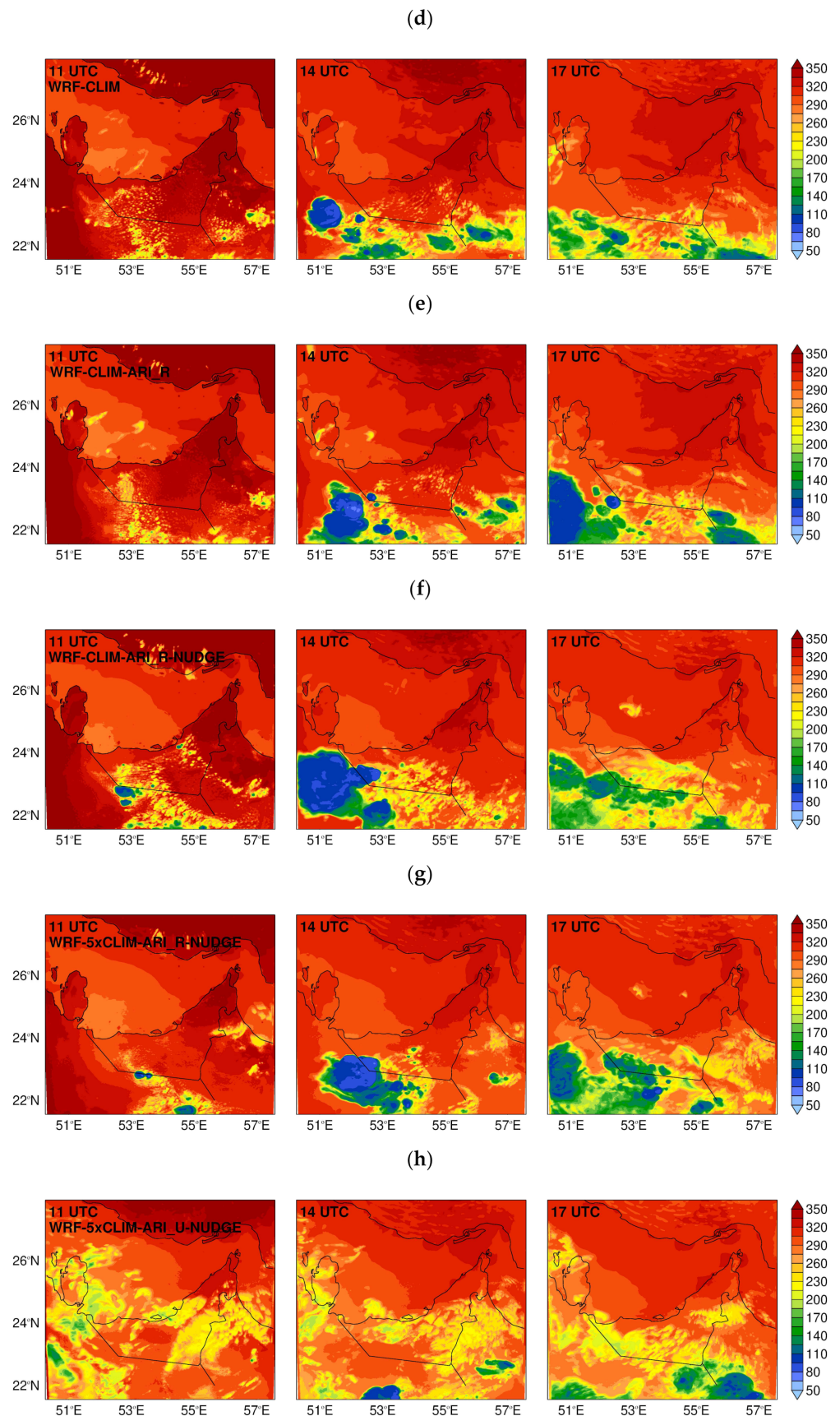


Figure 13. Cont.

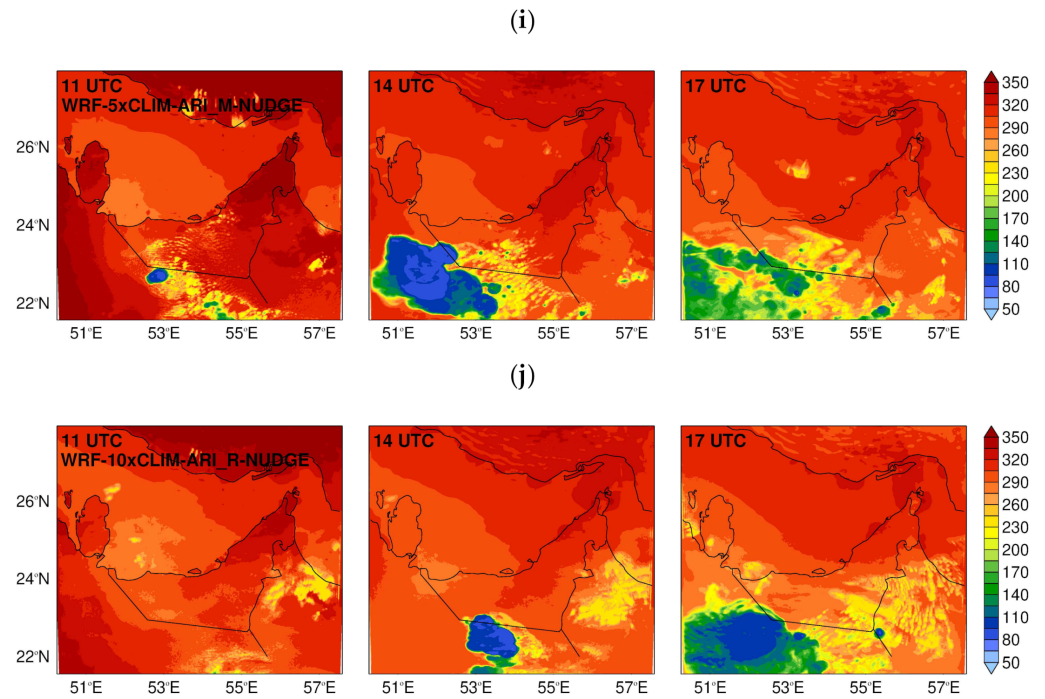


Figure 13. (a) IRBT (K) on 14 August 2013 at 11, 14 and 17 UTC. (b–j) Outgoing longwave radiation (OLR; $W m^{-2}$) on the same day and at the same times for all nine WRF simulations.

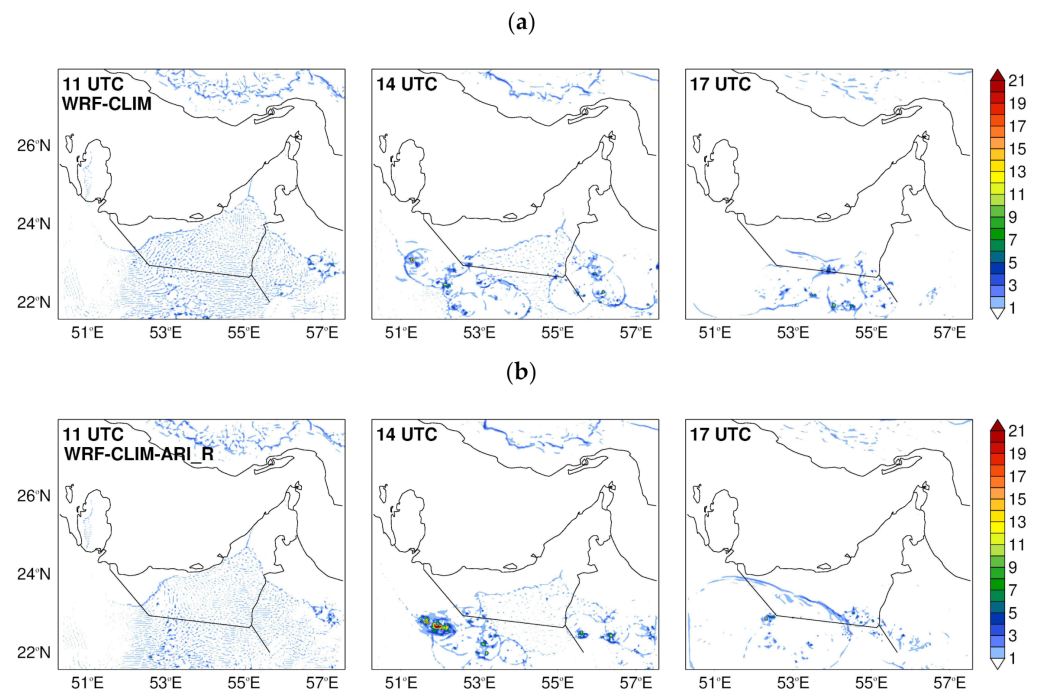


Figure 14. Cont.

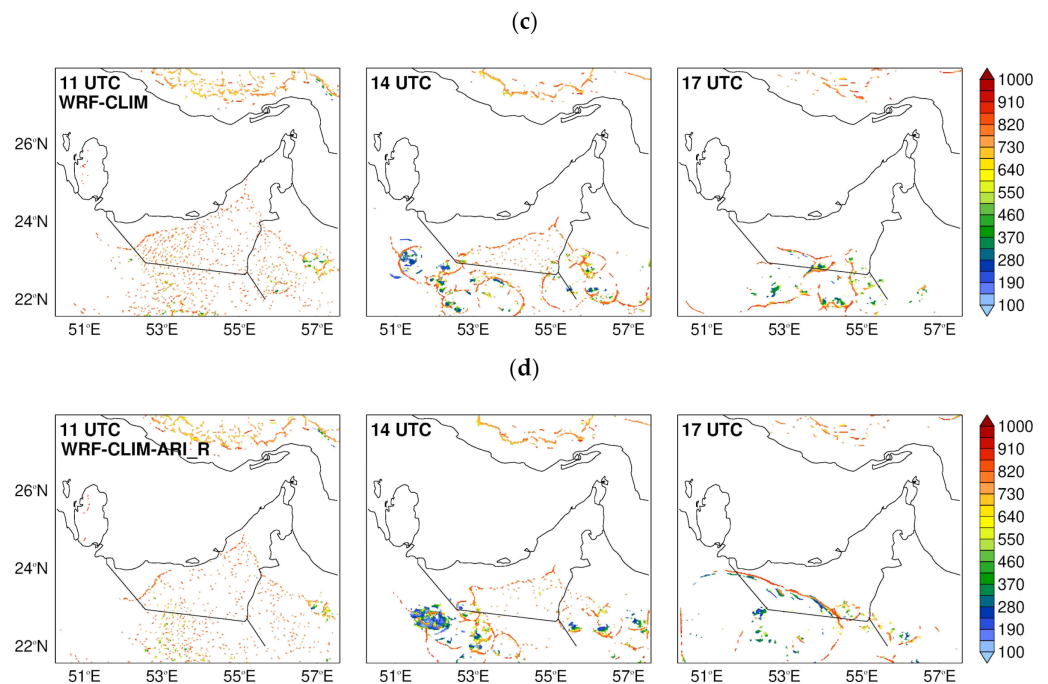


Figure 14. (a) Maximum vertical velocity (m s^{-1}) in the column of the 2.5 km WRF grid for the simulation WRF-CLIM. (b) is as (a) but for the WRF-CLIM-ARI_R run. (c,d) are as (a,b) but showing the pressure level (hPa) at which the maximum vertical velocity is observed.

The impact of the aerosol loading on the near-surface variables is summarized in Table 3. The main difference between runs WRF-CLIM-ARI_R-NUDGE, WRF-5 \times CLIM-ARI_R-NUDGE and WRF-10 \times CLIM-ARI_R-NUDGE is in the downward shortwave radiation flux, with a bias of about $+74 \text{ W m}^{-2}$, $+9 \text{ W m}^{-2}$ and -46 W m^{-2} , respectively. The other variables given in Table 3 show much reduced relative changes between runs WRF-CLIM-ARI_R-NUDGE, WRF-5 \times CLIM-ARI_R-NUDGE and WRF-10 \times CLIM-ARI_R-NUDGE. In fact, the 2 m temperature only decreases by about 0.5 K when the aerosol loading is increased by a factor of 10, a similar variation reported by [22] when the mineral dust emissions are doubled. The surface temperature, on the other hand, is roughly 6 K colder in WRF-10 \times CLIM-ARI_R-NUDGE compared with WRF-CLIM-ARI_R-NUDGE (not shown). In the surface layer scheme, the 2 m temperature is obtained from the surface temperature, the difference between the temperature at the first model level and the surface temperature, and the similarity function for heat [106]. The smaller change in air temperature may be attributed to the decrease in the sensible heat flux, by about 32 W m^{-2} , which leads to small changes in the temperature at the first model level and therefore in the 2 m temperature. As the NCM stations are spread out over the UAE (Figure 1) and as in some regions there is an increase in air temperature at certain times during the day due to drier conditions (Figure 16a), on average the variation will be small. The increase in the aerosol loading leads to warmer temperatures in the aerosol layer, with this being particularly evident at 12 UTC (Figure 11a), in particular below 700 hPa where the concentration of aerosols is higher (Figure 8b); the WRF temperature biases increase from $<0.5 \text{ K}$ in WRF-CLIM-ARI_R-NUDGE to up to 3 K in WRF-10 \times CLIM-ARI_R-NUDGE, and are accompanied by a drying of the layer by up to 15% (Figure 11b).

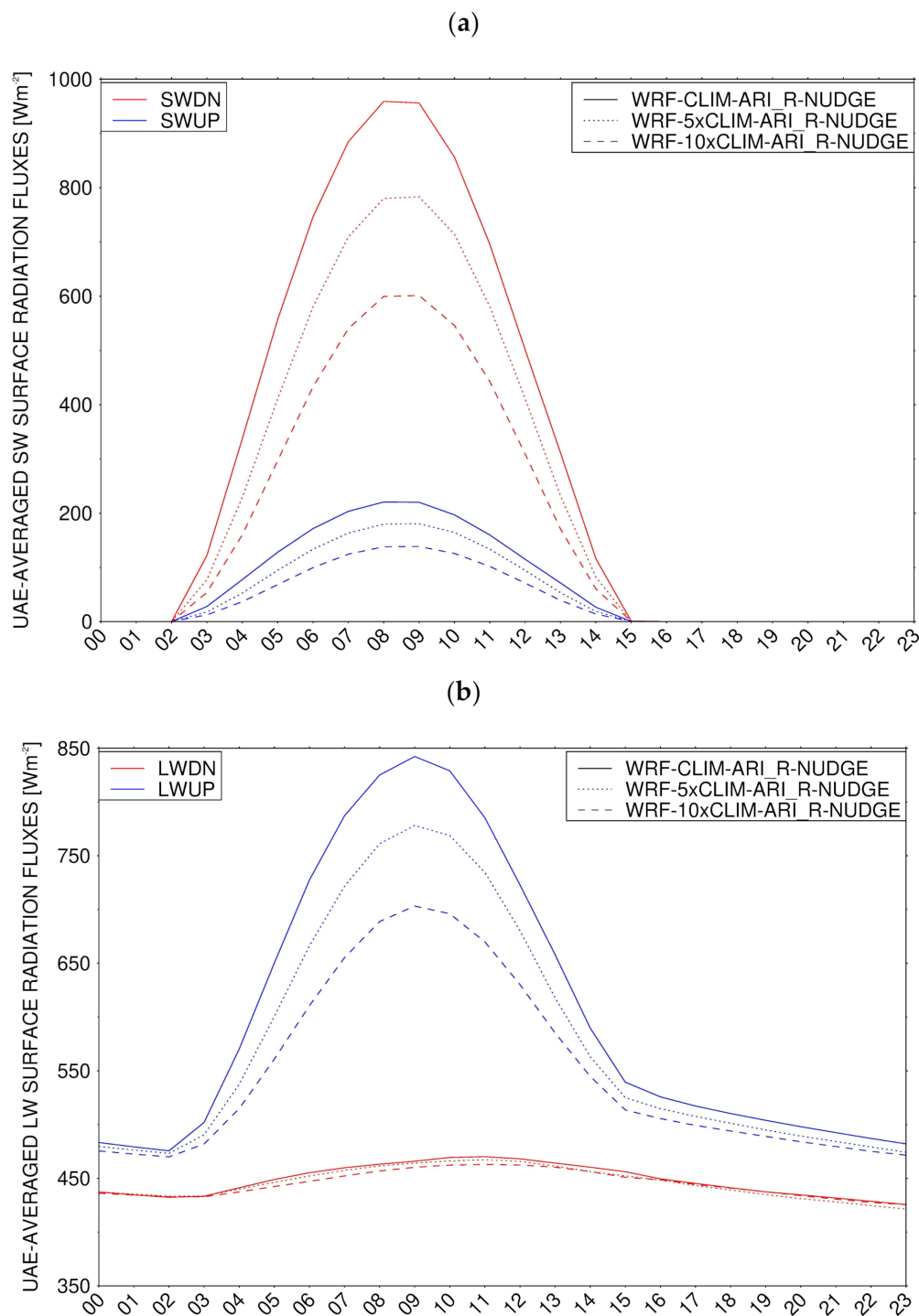


Figure 15. (a) UAE-averaged upward (red) and downward (blue) surface shortwave radiation flux ($W m^{-2}$) for 14 August 2013 for the simulations WRF-CLIM-ARI_R-NUDGE (solid line), WRF-5xCLIM-ARI_R-NUDGE (dotted line) and WRF-10xCLIM-ARI_R-NUDGE (dashed line). (b) is as (a) but for the longwave fluxes.

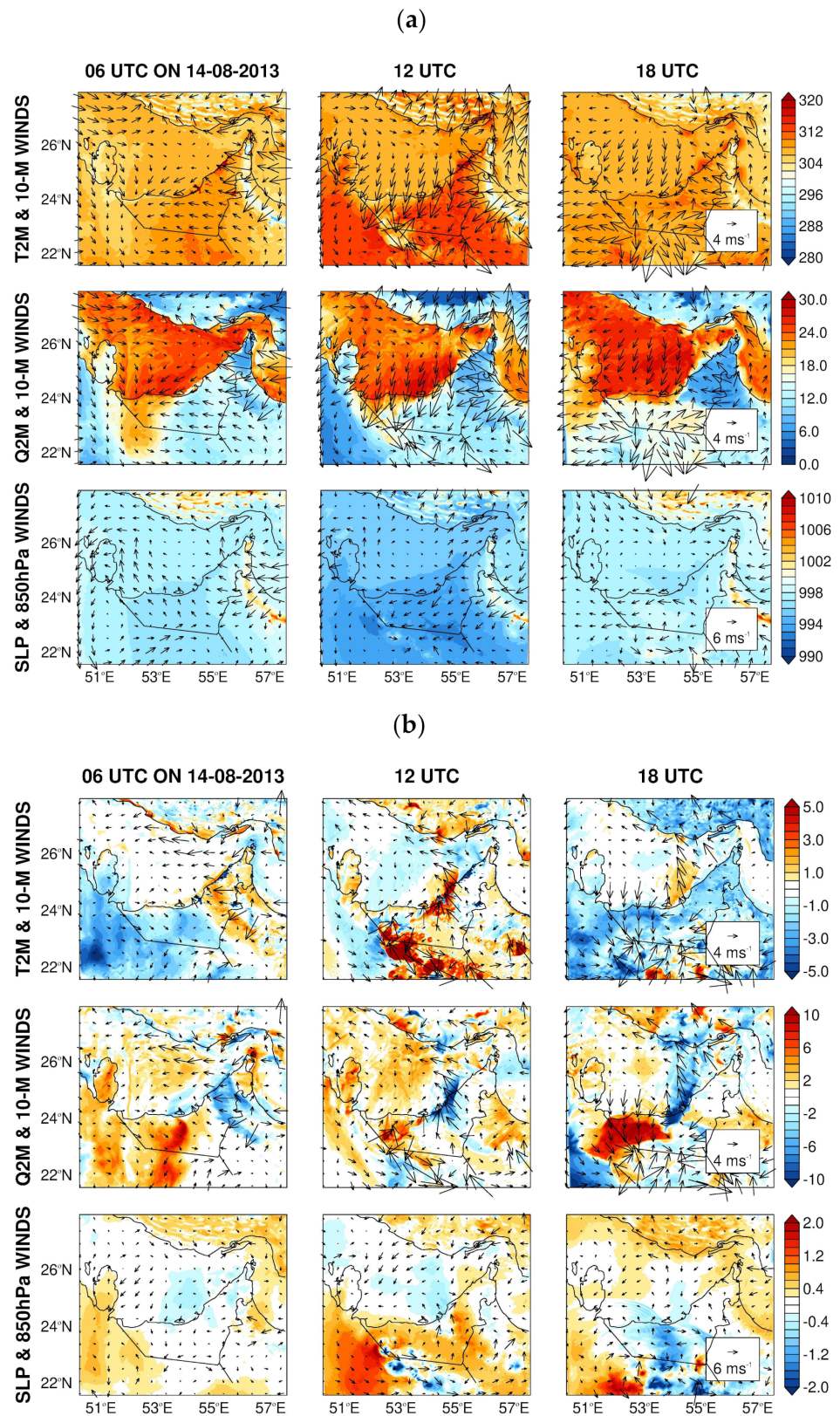


Figure 16. (a) The 2 m air temperature (K) and 10 m wind vector (m s^{-1}) (top row), 2 m water vapor mixing ratio (g kg^{-1}) and 10 m wind vector (m s^{-1}) (middle row), and sea-level pressure (hPa) and 850 hPa wind vector (m s^{-1}) (bottom row) on 14 August 2013 at 06, 12 and 18 UTC for the 2.5 km grid of the WRF-CLIM-ARI_R-NUDGE run. (b) is as (a) but showing the difference between the simulations WRF-10 \times CLIM-ARI_R-NUDGE and WRF-CLIM-ARI_R-NUDGE.

As the aerosol loading is increased, the model-predicted precipitation decreases. This is true at the location of the NCM stations (Table 3), and is easily seen in the accumulated precipitation maps (Figure 12f,g,j) with a domain-wise reduction of roughly 1% and 16% in WRF-5×CLIM-ARI_R-NUDGE and WRF-10×CLIM-ARI_R-NUDGE with respect to WRF-CLIM-ARI_R-NUDGE, respectively. This can be explained by the aerosols' impact on the atmospheric circulation. An inspection of Figure 16 reveals that in WRF-10×CLIM-ARI_R-NUDGE the AHL is displaced to the east, with the associated circulation leading to a deeper inland penetration of the moist Arabian Gulf air over western UAE and adjacent Saudi Arabia, while the southeasterly winds ahead of it slow down the sea-breeze progression and lead to drier conditions over parts of central and eastern UAE. Despite an aerosol loading that is 10 times higher, the drier environment here, with differences in the water vapor mixing ratio of more than 10 g kg^{-1} , allows for warmer air temperatures, spreading into parts of the Gulf at 18 UTC. However, elsewhere it is colder in WRF-10×CLIM-ARI_R-NUDGE when compared to WRF-CLIM-ARI_R-NUDGE, in particular at 18 UTC. The reduced spatial extent and amount of precipitation in WRF-10×CLIM-ARI_R-NUDGE arises from an eastward shift in the region of low-level wind convergence, into an area where the atmosphere is drier. Figure 16 highlights the importance of the aerosols' effects on the model-predicted circulation (and consequently on the precipitation) which are more prominent for higher aerosol loadings, a finding also reached by [107] for simulations over northern India in the 2008 summer monsoon. Besides the suppressed rainfall, there is also a delay in the development of convective clouds as the aerosol loading is increased, as seen by comparing Figure 13f,g,j.

4.2.3. Sensitivity to Aerosol Properties

In Section 4.2.2, the impact of the aerosol loading on the surface fluxes and atmospheric circulation is investigated. Here, the focus will be on the aerosol properties, with the aerosol loading in all simulations corresponding to that of the climatological distribution scaled by a factor of 5, which has been found to give the best agreement with the MERRA-2-predicted AOD averaged over the UAE (Figure 9). The results are summarized in Figures 17 and 18 and in Table 3.

As stated in Section 2.2, and due to the presence of carbonaceous particles, the urban aerosol model (WRF-5×CLIM-ARI_U-NUDGE) is more absorbing than the rural (default) model (WRF-5×CLIM-ARI_R-NUDGE), while the maritime aerosol model (WRF-5×CLIM-ARI_M-NUDGE) is less absorbing as the larger particles are removed and some of the rural aerosols are replaced with sea salt. The results in Figure 17 show that a change in the aerosol composition has a larger impact on the surface radiation fluxes than an increase in the aerosol loading (cf., Figure 15). In particular, when the urban aerosol model is used, the downward shortwave radiation flux is cut by up to 360 W m^{-2} with a daily average reduction of around 114 W m^{-2} , a larger radiative effect than when the aerosol loading is multiplied by a factor of 10. The important role played by the aerosol composition has also been highlighted by [66] for WRF simulations over Borneo. When compared with WRF-5×CLIM-ARI_U-NUDGE, the reduction in the upward longwave radiation flux exceeds 100 W m^{-2} , and is a result of the much colder surface, with the daily averaged surface temperature dropping by about 7 K (not shown) and the air temperature by 0.8 K (Table 3). The radiation absorbed by the aerosols during the day is emitted at night, and in the urban aerosol model the aerosols are so absorbing that the surface downward longwave radiation flux in WRF-5×CLIM-ARI_U-NUDGE is up to 12 W m^{-2} higher than in WRF-5×CLIM-ARI_R-NUDGE at night (Figure 17b). The impact of changing aerosol properties on the temperature and RH vertical profiles is given in Figure 11. The most noteworthy difference between simulations WRF-5×CLIM-ARI_R-NUDGE and WRF-5×CLIM-ARI_U-NUDGE is the heating around 700–750 hPa and the cooling below 800 hPa in simulation WRF-5×CLIM-ARI_U-NUDGE at 12 UTC, with magnitudes up to +1.5 K and −3.5 K, respectively. As the urban aerosols are more absorbing, and most are below 700 hPa at this time of the day (Figure 8b), there is a strong heating at the top of the layer and a cooling

at lower levels as the vast majority of the incoming solar radiation is absorbed. This is in contrast to when the aerosol loading is increased, where the most pronounced warming occurs in the lowest part of the layer.

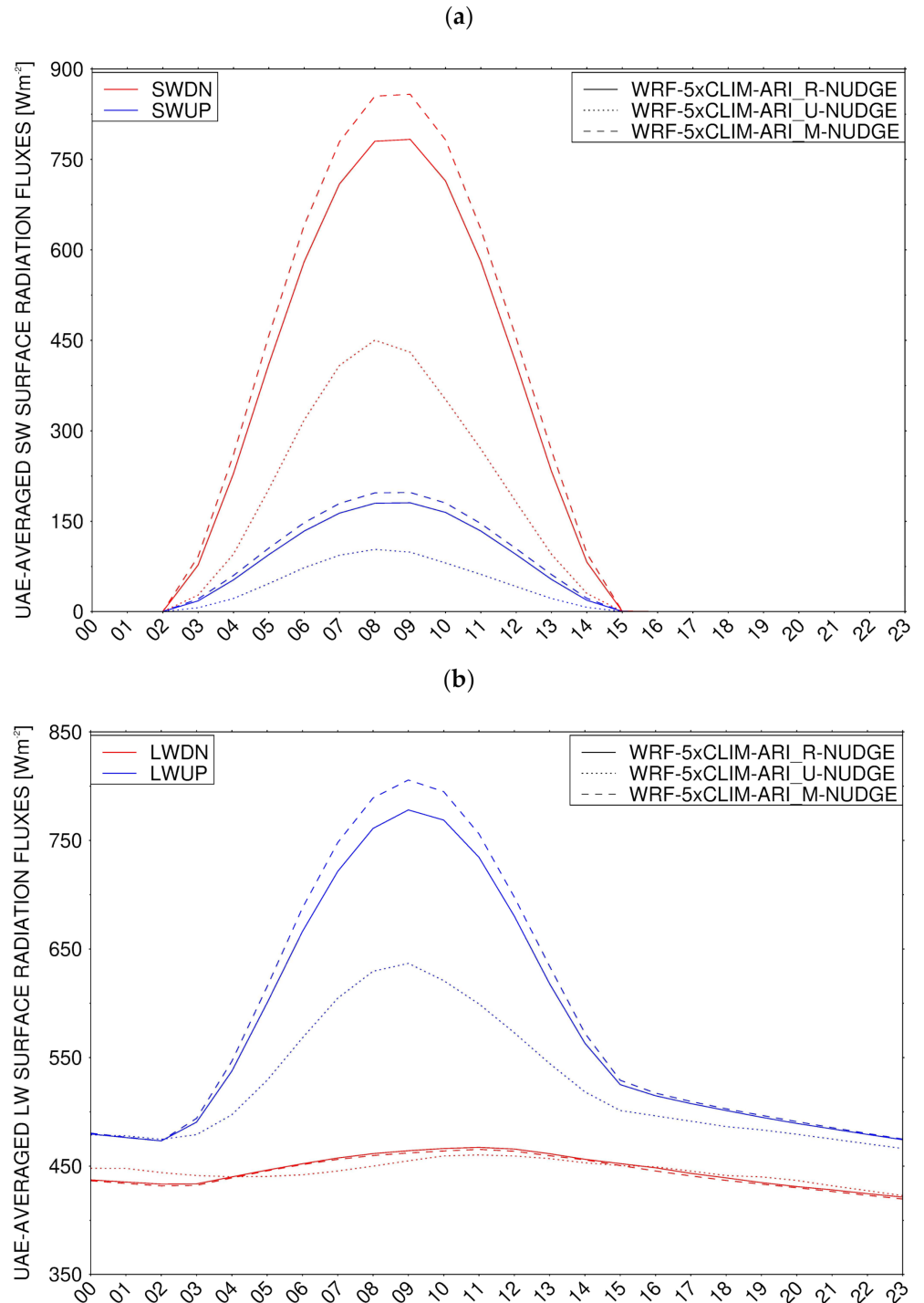


Figure 17. (a) UAE-averaged upward (red) and downward (blue) surface shortwave radiation flux ($W m^{-2}$) for 14 August 2013 for the simulations WRF-5xCLIM-ARI_R-NUDGE (solid line), WRF-5xCLIM-ARI_U-NUDGE (dotted line) and WRF-10xCLIM-ARI_M-NUDGE- (dashed line). (b) is as (a) but for the longwave fluxes.

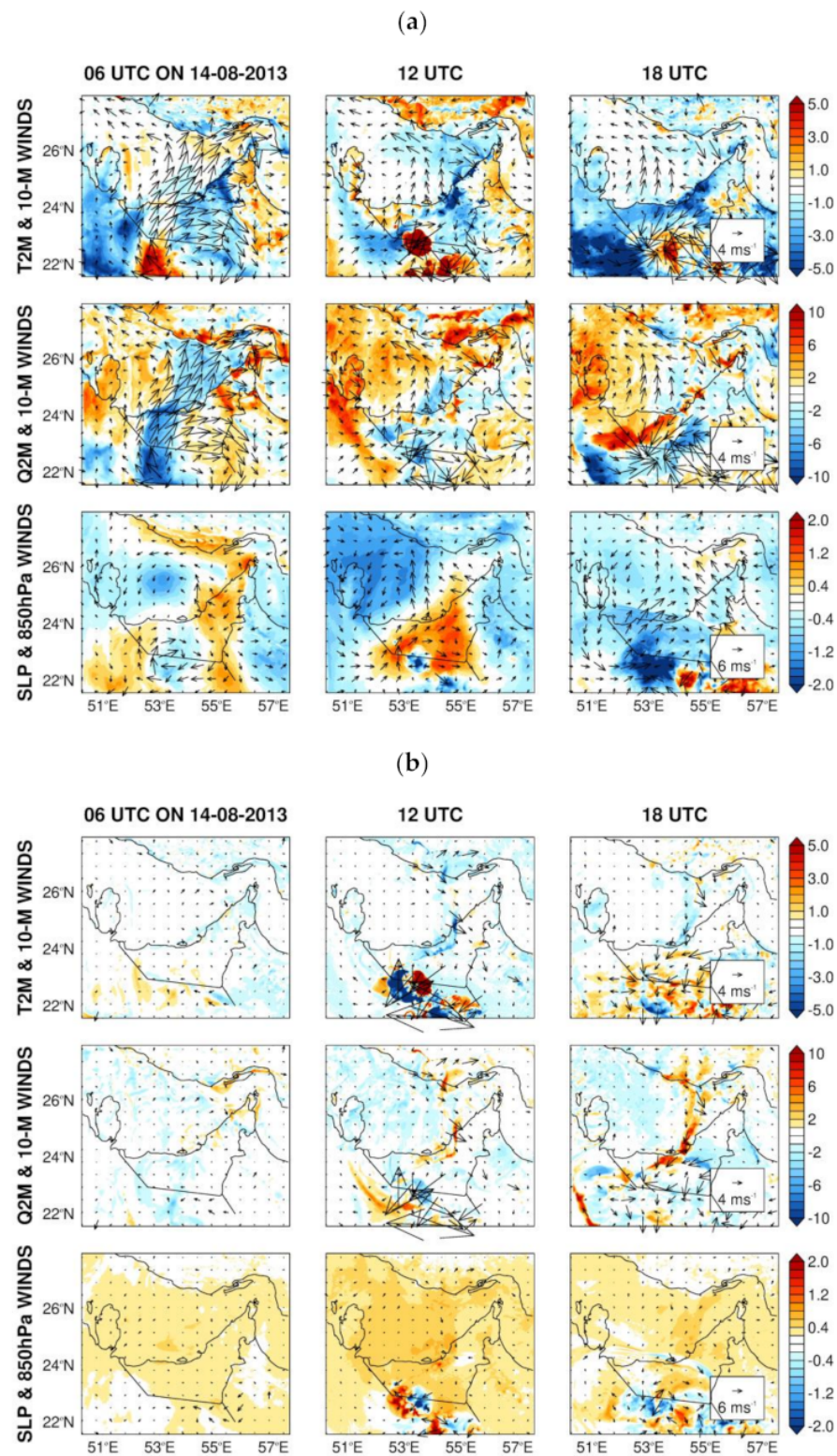


Figure 18. Differences in the 2 m air temperature (K) and 10 m wind vector (m s^{-1}) (top row), 2 m water vapor mixing ratio (g kg^{-1}) and 10 m wind vector (m s^{-1}) (middle row), and sea-level pressure (hPa) and 850 hPa wind vector (m s^{-1}) (bottom row) on 14 August 2013 at 06, 12 and 18 UTC for the for the 2.5 km grid between the (a) WRF-5×CLIM-ARI_U-NUDGE and WRF-5×CLIM-ARI_R-NUDGE simulations and the (b) WRF-5×CLIM-ARI_M-NUDGE and WRF-5×CLIM-ARI_R-NUDGE simulations.

The impact of making the aerosols more absorbing on the atmospheric circulation is presented in Figure 18. When carbonaceous aerosols are added, the AHL is weaker (note the anticyclonic circulation in the 10 m winds at 06 UTC and to a lesser extent at 12 UTC) and broader, as evidenced by the negative sea-level pressure anomalies over the Arabian Gulf and Oman, in WRF-5×CLIM-ARI_U-NUDGE when compared with WRF-5×CLIM-ARI_R-NUDGE. This is consistent with the referred pronounced reduction in the downward shortwave radiation flux and resulting colder surface and air temperatures (Table 3). As the land temperatures become more comparable to the sea surface skin temperatures over the Gulf, the sea-level pressure minimum extends into adjacent areas, which allows the AHL to expand. As a result of the modifications to the AHL, the excessive moistening over western UAE is reduced, and increased over eastern and southeastern parts of the country. The interaction between the associated cyclonic circulation and the sea-breeze from the Sea of Oman and Arabian Gulf leads to a region of low-level wind convergence here where, due to a moister environment, the model predicts precipitation (Figure 12h). WRF-5×CLIM-ARI_U-NUDGE is the wettest simulation over the UAE, with roughly 35% of the observed precipitation at the location of the NCM stations captured by the model (Table 3). However, a comparison of Figure 13g,h reveals that the rainfall falls from shallower clouds, with deep convection virtually absent in this simulation. The weakening of the AHL also brings it closer to that given by ERA-5, Figure 7b.

When the maritime aerosol model is used, on the other hand, there is a small increase in the downward shortwave radiation flux by up to 75 W m^{-2} , or by $\sim 22 \text{ W m}^{-2}$ on a daily averaged scale, with the surface temperature at the location of the NCM stations higher by about 1 K (not shown). The AHL is slightly weaker and smaller in size in this run (Figure 18b), with the changes in sea-level pressure mostly within 1 hPa, whereas in WRF-5×CLIM-ARI_U-NUDGE in some regions they exceed 2 hPa. As a result, the precipitation and the clouds shift southwards with respect to those in WRF-5×CLIM-ARI_R-NUDGE (Figure 12g,i and Figure 13g,i), with less rainfall accumulated at the location of the NCM stations (Table 3).

5. Discussion and Conclusions

In this manuscript, the Weather Research and Forecasting (WRF) model is used to investigate the role of aerosol loading and properties in a dusty summertime convective event in the United Arab Emirates (UAE), which occurred on 14 August 2013. This convective event was triggered by the low-level convergence of the cyclonic circulation associated with the Arabian Heat Low (AHL), located over western UAE, and the sea-breeze from the Arabian Gulf and Sea of Oman. This was also a rather dusty day in the UAE, with Aerosol Optical Depths (AODs) in excess of two. An analysis of reanalysis data revealed that two factors played a role in the dust-lifting activities on this day: (i) cold pools and downbursts, which occurred in association with the convective activity in the local afternoon and evening hours, and (ii) strong near-surface winds along the leading edge of the Intertropical Discontinuity (ITD) earlier in the day.

The main findings of this work are as follows:

1. Two aerosol distributions are considered in this study: an idealized distribution, set up for the continental United States, and a climatological profile, based on a 7-year output of a general circulation model. The best agreement is found when the climatological values are multiplied by a factor of 5, in line with the dustier atmosphere during this event.
2. For the simulations with the idealized and climatological aerosol distributions, when the aerosol–radiation interaction (ARI) effects are switched on, the daily averaged surface downward shortwave radiation flux is reduced by 3 W m^{-2} and 20 W m^{-2} , respectively, leading to changes in the surface temperature within 1 K and in the air temperature within 0.5 K. Activating the ARI effects when the climatological aerosol loading is used leads to a roughly 47% increase in the domain-wide precipitation, as

the convective cells are more active, and the stronger updrafts increase the fraction of activated aerosols.

3. WRF has a cold bias over the UAE, which is not alleviated when interior nudging in the outermost and two outermost grids is employed. While the skill scores of the innermost nest improved in particular when interior nudging is applied to the two outermost grids, the cold bias in the 2.5 km grid persisted. This is because a change in the atmospheric circulation, in particular in the position of the AHL, leads to increased precipitation over the UAE and locally colder temperatures, which offset the higher temperatures that arise from more accurate boundary conditions.
4. The downward and upward shortwave and the upward longwave radiation fluxes are found to decrease linearly as the aerosol loading is increased. As the aerosol loading goes up, the AHL shifts eastwards, with the low-level wind convergence taking place in a drier region, resulting in lower precipitation amounts falling in a more spatially confined area. In addition, the onset of convection is also delayed.
5. When 20% of the aerosols are replaced with more absorbing (carbonaceous) particles, the roughly 87 W m^{-2} decrease in the surface net shortwave radiation flux is comparable to the drop when the aerosol loading is augmented by a factor of 10. This stresses that the aerosol composition plays a role as important as its amount on the surface radiative fluxes, at least for the range of values considered here.

Even though, in a comparison with observed measurements, no simulation clearly outperformed another, the sensitivity experiments highlighted aspects of the experimental setup that have to be carefully considered for aerosol-related simulations in hyperarid regions adjacent to major aerosol sources such as the UAE:

1. When accounting for the observed aerosol loading, using a climatology-based distribution is preferable to an idealized distribution as it can improve the representation of deep convection.
2. Even in the short term, such as 2-day simulations, the fields in the interior of the WRF nests can be substantially different from those in the input dataset. Employing nudging in the outer nests is preferable to only applying it in the outermost nest or not doing it altogether, as it helps to at least partially correct some of the WRF biases.
3. It is vital to accurately represent the properties of the observed aerosols in the model, more so than the amount, provided the order of magnitude is in line with that observed.

The representation of ARI and aerosol–cloud interaction (ACI) effects in the model still needs to be further refined, in particular with respect to the aerosol optical properties and size distribution. This can be achieved through additional studies that combine both in situ measurements (such as aerosol concentration profiles from aircraft measurements; [89]) and numerical modelling. An extension of this work would be to investigate whether similar findings are reached for summertime convective events that occur on the eastern side of the UAE, for which the AHL plays a reduced role in the triggering of the convective clouds [19]. It is also of interest to further explore the interaction between the ARI and ACI effects and the background meteorological state. This can be achieved through the piggybacking methodology [108], where two sets of thermodynamic variables, one coupled with the model dynamics and another applied diagnostically (i.e., driven by the flow but not feedbacking into it), are considered.

Author Contributions: Conceptualization, D.F.; Methodology, R.F., D.F. and N.N.; software, S.F., Y.W., T.A., O.T. and R.M.; validation, R.F., D.F., M.W. and N.N.; formal analysis, M.W., N.N., S.F., Y.W., T.A., O.T. and R.M.; investigation, R.F., D.F. and N.N.; resources, D.F., S.F., Y.W., T.A., O.T. and R.M.; data curation, R.F., M.W. and N.N.; writing—original draft preparation, R.F. and D.F.; visualization, R.F. and N.N.; supervision, D.F.; project administration, D.F. All authors have read and agreed to the published version of the manuscript.

Funding: This research was funded by UAEREP, project number 8434000263.

Institutional Review Board Statement: Not applicable.

Informed Consent Statement: Not applicable.

Data Availability Statement: The station data and the UAE-optimized WRF model are archived at the National Center of Meteorology. Readers can request the data and the model codes by contacting research@ncms.ae. All other datasets used in this study are freely available online and the links are provided in the Acknowledgements.

Acknowledgments: This work is supported by the National Center of Meteorology (NCM), Abu Dhabi, United Arab Emirates (UAE), under the UAE Research Program for Rain Enhancement Science (UAEREP). The authors thank the NCM for providing the weather station and air quality observations over the UAE, under an agreement with clauses for non-disclosure of data. Access to these data is restricted and readers should request them through contacting research@ncms.ae. We would also like to thank the UAE NCM for kindly providing radiosonde data at Abu Dhabi's International Airport through the National Oceanic and Atmospheric Administration Integrated Global Radiosonde Archive's website (<https://www.ncei.noaa.gov/products/weather-balloon/integrated-global-radiosonde-archive>, accessed on 8 August 2021). The Spinning Enhanced Visible and Infrared Imager data were extracted from The European Organisation for the Exploitation of Meteorological Satellites' website (<https://eoportal.eumetsat.int/>, accessed on 8 August 2021); the Infrared Brightness Temperature data were downloaded from the National Aeronautic and Space Administration's website (https://disc.gsfc.nasa.gov/datasets/GPM_MERGIR_1/summary, accessed on 8 August 2021) as was the case for the MERRA-2 data (<https://disc.gsfc.nasa.gov/datasets?project=MERRA-2>, accessed on 8 August 2021); the ERA-5 data are available on the European Centre for Medium Range Weather Forecast's Copernicus website (<https://cds.climate.copernicus.eu/>, accessed on 8 August 2021). The authors also wish to acknowledge the major contribution of Khalifa University's high-performance computing and research facilities to the results of this research. We are also grateful to the four anonymous reviewers of this work for their detailed and insightful comments and suggestions which helped to significantly improve the quality of the manuscript.

Conflicts of Interest: The authors declare no conflict of interest.

Appendix A. Sensitivity to Nudging Formulation

WRF has a considerable cold bias over hyperarid regions, which is not restricted to the UAE. However, when ERA-5 data, used to force the model, are compared with station data, such a cold bias is much reduced; it is mostly within 1 K and with a maximum value of 2.7 K, less than half of the peak WRF bias (Figure 10). As attempts to address this issue by modifying the WRF configuration have not been successful [48,95,96], interior nudging towards ERA-5 was applied to the outermost and two outermost grids in an attempt to correct the aforementioned model biases. As noted in Section 2.2, the fields nudged include the water vapor mixing ratio, temperature, and horizontal wind components above 800 hPa and on a timescale of 1 h, excluding the PBL. Figure A1 shows near-surface atmospheric fields for the run with the climatological aerosol loading and without interior nudging, WRF-CLIM-ARI_R, and the difference between the two simulations with interior nudging and this control run.

When interior nudging is employed in the 22.5 km and 7.5 km grids, WRF-CLIM-ARI_R-NUDGE, the model predictions in the 2.5 km grid are generally more skilful when compared with the run where no interior nudging is applied (Table 3) or when it is restricted to the 22.5 km grid (not shown), as the output of the 7.5 km grid is used to generate boundary conditions for the innermost nest. In particular, a comparison of Figures A1a,c and 7b reveals that the near-surface fields in the 2.5 km grid are corrected towards those in ERA-5, despite the fact that the interior nudging is only applied above 800 hPa and in the outer grids. As an example, the atmosphere over central and western UAE is moister at 06 UTC and over the UAE it is generally warmer as well; the minimum sea-level pressure is shifted eastwards at this time, closer to that in ERA-5; at 12 and 18 UTC, the sea-level pressures are higher in WRF-CLIM-ARI_R-NUDGE compared with WRF-CLIM-ARI_R. These tendencies are also present when nudging is restricted to the outermost grid but are of a smaller magnitude, as the ERA-5 signal is likely weakened by the lack of interior nudging in the intermediate grid. These results are consistent with the findings of [69], who concluded that employing analysis nudging in the interior of 30 km and 10 km grids of a three-nest simulation leads to more accurate predictions in the 2 km innermost grid compared to when interior nudging is restricted to the 30 km grid.

Table 3 shows that in WRF-CLIM-ARI_R-NUDGE, the aforementioned cold bias is slightly reduced, albeit by only 0.01 K on a daily averaged scale. This is because WRF also generates more precipitation, which leads to locally colder temperatures (cf., Figure A1c). In both nudging simulations, the AHL is displaced to the east with respect to WRF-CLIM-ARI_R, in particular when nudging is employed in the two outermost grids, with the low-level convergence of the associated cyclonic circulation with the sea-breeze from the Arabian Gulf leading to increased rainfall over central and eastern UAE (Figure 12e,f). On the backside of the AHL, the enhanced moisture advection from the Arabian Gulf augments the precipitation over southwestern UAE and adjacent Saudi Arabia, as evidenced by the deeper convection in the region (Figure 13e,f). Over northeastern UAE, on the other hand, the southeasterly winds from the AHL bring in drier air from the desert and weaken the moistening effect of the sea breeze from the Sea of Oman and Arabian Gulf, leading to a reduction in the 2 m water vapor mixing ratio by more than 10 g kg^{-1} at some sites in WRF-CLIM-ARI_R-NUDGE. As a result, the averaged bias of this field at the location of the NCM stations increases slightly from -2.32 g kg^{-1} in simulation WRF-CLIM-ARI_R to -2.81 g kg^{-1} in WRF-CLIM-ARI_R-NUDGE. The air temperature, sea-level pressure, downward shortwave radiation and precipitation scores, on the other hand, are higher for WRF-CLIM-ARI_R-NUDGE compared with WRF-CLIM-ARI_R (Table 3). A marginal improvement is also seen in the vertical profiles of temperature and RH with respect to the Abu Dhabi sounding data (Figure 11). With respect to WRF-CLIM-ARI_R (cyan curve), in WRF-CLIM-ARI_R-NUDGE (dark green curve) there is a slight reduction in the biases; for example, note the decrease in the air temperature biases around 500 hPa and 850–950 hPa at 00 UTC and between 150 and 350 hPa at 12 UTC by up to 1 K, and in the RH biases between 550 and 700 hPa at 12 UTC by up to 10%.

In summary, while the application of interior nudging in the outermost or two outermost grids generally improves the model performance, in line with the findings of other studies, in some regions (e.g., northeastern UAE) it may have detrimental effects, due to its impact on the atmospheric circulation. Nevertheless, simulation WRF-CLIM-ARI_R-NUDGE is preferred to WRF-CLIM-ARI_R, as per the scores given in Table 3, with this nudging configuration recommended for summertime convection simulations in this region.

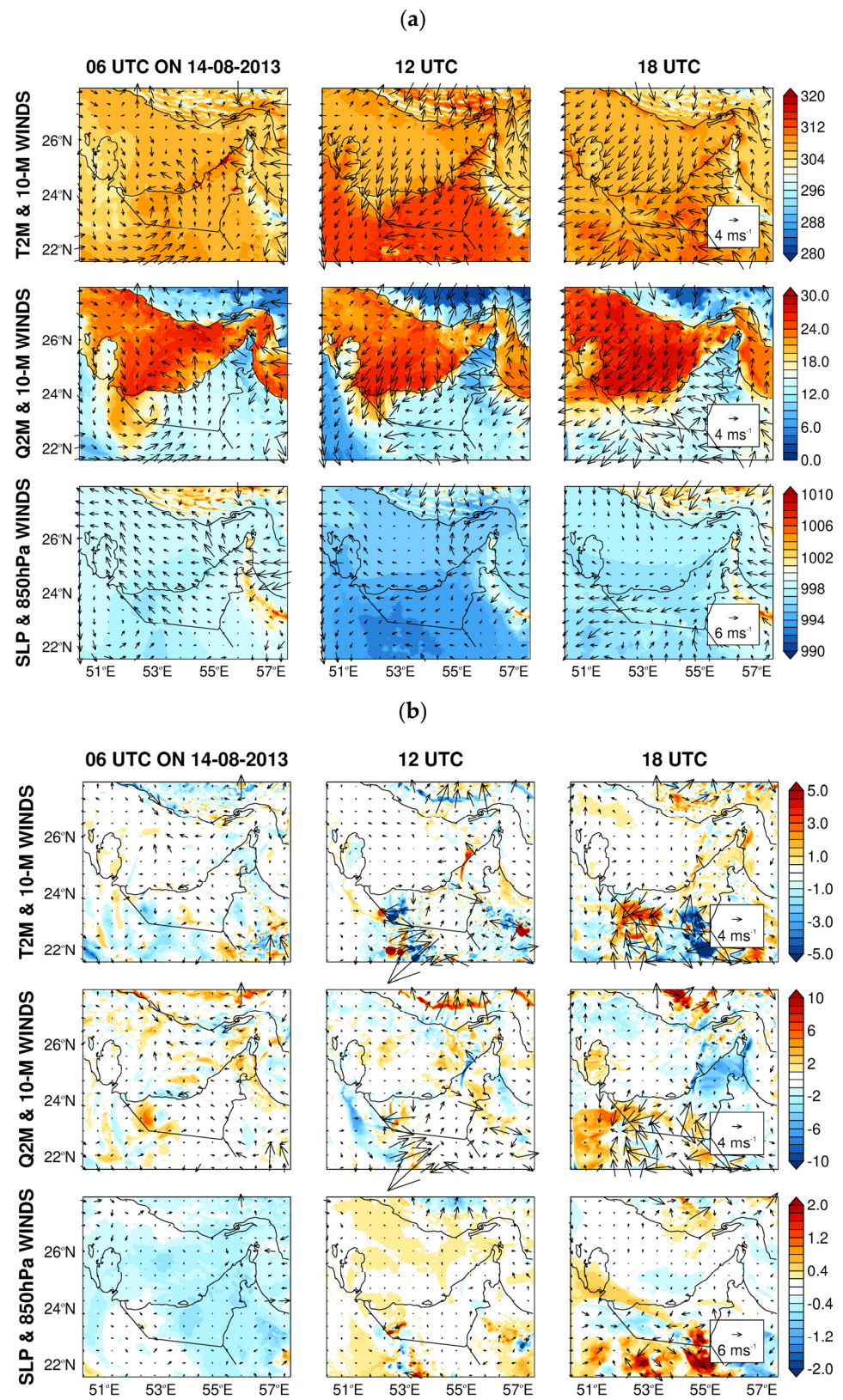


Figure A1. Cont.

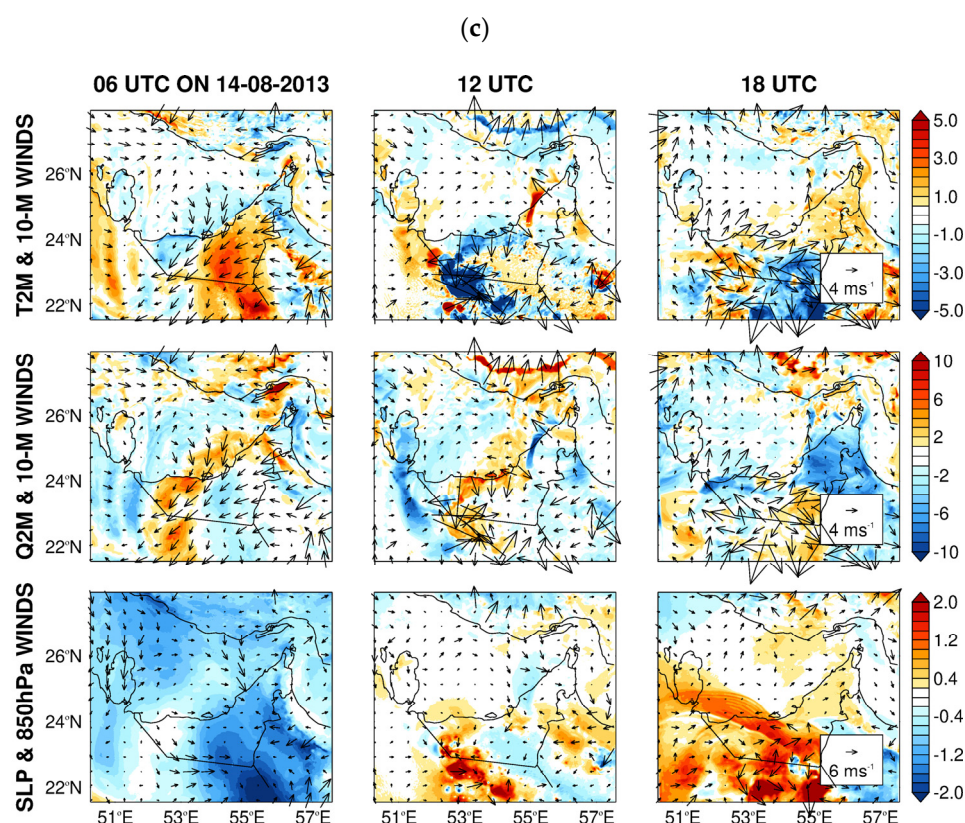


Figure A1. (a) The 2 m air temperature (K) and 10 m wind vector (m s⁻¹) (top row), 2 m water vapor mixing ratio (g kg⁻¹) and 10 m wind vector (m s⁻¹) (middle row), and sea-level pressure (hPa) and 850 hPa wind vector (m s⁻¹) (bottom row) on 14 August 2013 at 06, 12 and 18 UTC for the 2.5 km grid of the WRF-CLIM-ARI_R simulation. (b,c) are as (a) but showing the differences between the runs where nudging is only employed in the outermost grid and in the two outermost nests (WRF-CLIM-ARI_R-NUDGE) and WRF-CLIM-ARI_R, respectively.

References

- Ramanathan, V.; Crutzen, P.J.; Kiehl, J.T.; Rosenfeld, D. Aerosols, Climate, and the Hydrological Cycle. *Science* **2001**, *294*, 2119–2124. [[CrossRef](#)]
- Choobari, O.A.; Zawar-Reza, P.; Sturman, A. The global distribution of mineral dust and its impacts on the climate system: A review. *Atmos. Res.* **2014**, *138*, 152–165. [[CrossRef](#)]
- Boucher, O. Atmospheric Aerosols. In *Atmospheric Aerosols*; Springer: Dordrecht, The Netherlands, 2015. Available online: https://doi.org/10.1007/978-94-017-9649-1_2 (accessed on 16 September 2021).
- Satheesh, S.K.; Moorthy, K.K. Radiative effects of natural aerosols: A review. *Atmos. Environ.* **2005**, *39*, 2089–2110. [[CrossRef](#)]
- Wang, W.; Huang, J.; Minnis, P.; Hu, Y.; Li, J.; Huang, Z.; Ayers, J.K.; Wang, T. Dusty cloud properties and radiative forcing over dust source and downwind regions derived from A-Train data during the Pacific Dust Experiment. *J. Geophys. Res. Atmos.* **2010**, *115*, D00H35. [[CrossRef](#)]
- Li, Z.; Wang, Y.; Guo, J.; Zhao, C.; Cribb, M.C.; Dong, X.; Fan, J.; Gong, D.; Huang, J.; Jiang, M.; et al. East Asian study of tropospheric aerosols and their impact on regional clouds, precipitation, and climate (EAST-AIR(CPC)). *J. Geophys. Res.* **2019**, *124*, 13026–13054. [[CrossRef](#)]
- Lohmann, U.; Feichter, J. Global indirect aerosol effects: A review. *Atmos. Chem. Phys.* **2005**, *5*, 715–737. [[CrossRef](#)]
- Twomey, S.A.; Piepgrass, M.; Wolfe, T.L. An assessment of the impact of pollution on global cloud albedo. *Tellus B* **1984**, *36*, 356–366. [[CrossRef](#)]
- Albrecht, B.A. Aerosols, Cloud Microphysics, and Fractional Cloudiness. *Science* **1989**, *245*, 1227–1230. [[CrossRef](#)]
- Kok, J.F.; Abediyi, A.A.; Albani, S.; Balkansi, Y.; Checa-Garcia, R.; Chin, M.; Colarco, P.R.; Hamilton, D.S.; Huang, Y.; Ito, A.; et al. Contribution of the world's main dust source regions to the global cycle of desert dust. *Atmos. Chem. Phys.* **2021**, *21*, 8169–8193. [[CrossRef](#)]
- Francis, D.; Eayrs, C.; Chaboureaud, J.-P.; Mote, T.; Holland, D.M. A meandering polar jet caused the development of a Saharan cyclone and the transport of dust toward Greenland. *Adv. Sci. Res.* **2019**, *16*, 49–56. [[CrossRef](#)]
- Tegen, I.; Schepanski, K. The global distribution of mineral dust. *IOP Conf. Ser. Earth Environ. Sci.* **2009**, *7*, 012001. [[CrossRef](#)]

13. Min, Q.-L.; Li, R.; Lin, B.; Joseph, E.; Morris, V.; Hu, Y.; Li, S.W.; Wang, S. Impacts of mineral dust on ice clouds in tropical deep convection systems. *Atmos. Res.* **2014**, *143*, 64–72. [[CrossRef](#)]
14. Liu, Y.; Zhu, Q.; Huang, J.; Hua, S.; Jia, R. Impact of dust-polluted convective clouds over the Tibetan Plateau on downstream precipitation. *Atmos. Environ.* **2019**, *209*, 67–77. [[CrossRef](#)]
15. Francis, D.; Chaboureaud, J.-P.; Nelli, N.; Cuesta, J.; Al Shamsi, N.; Temimi, M.; Pauluis, O.; Xue, L. Summertime dust storms over the Arabian Peninsula and impacts on radiation, circulation, cloud development and rain. *Atmos. Res.* **2020**, *250*, 105364. [[CrossRef](#)]
16. Evan, A.T.; Foltz, G.R.; Zhang, D. Physical Response of the Tropical-Subtropical North Atlantic Ocean to Decadal-Multidecadal Forcing by African Dust. *J. Clim.* **2012**, *25*, 5817–5829. [[CrossRef](#)]
17. Huang, C.-C.; Chen, S.-H.; Lin, Y.-C.; Earl, K.; Matsui, T.; Lee, H.-H.; Tsai, I.-C.; Chen, J.-P.; Cheng, C.-T. Impacts of Dust-Radiation versus Dust-Cloud Interactions on the Development of a Modeled Mesoscale Convective System over North Africa. *Mon. Weather Rev.* **2019**, *147*, 3301–3326. [[CrossRef](#)]
18. Skamarock, W.C.; Klemp, J.B.; Dudhia, J.; Gill, D.O.; Liu, Z.; Berner, J.; Wang, W.; Powers, J.G.; Duda, M.G.; Barker, D.; et al. *A Description of the Advanced Research WRF Model Version 4 (No. NCAR/TN-556+STR)*; National Center for Atmospheric Research: Boulder, CO, USA, 2019; 6p.
19. Francis, D.; Temimi, M.; Fonseca, R.; Nelli, N.R.; Abida, R.; Weston, M.; Whebe, Y. On the analysis of a summertime convective event in a hyperarid environment. *Q. J. R. Meteorol. Soc.* **2021**, *147*, 501–525. [[CrossRef](#)]
20. Liu, L.; Cheng, Y.; Wang, S.; Wei, C.; Pohlker, M.L.; Pohlker, C.; Artaxo, P.; Shrivastava, M.; Andreae, M.O.; Poschl, U.; et al. Impact of biomass burning aerosols on radiation, clouds, and precipitation over the Amazon: Relative importance of aerosol–cloud and aerosol–radiation interactions. *Atmos. Chem. Phys.* **2020**, *20*, 13283–13301. [[CrossRef](#)]
21. Grell, G.A.; Peckham, S.E.; Schmitz, R.; McKeen, S.A.; Frost, G.; Skamarock, W.C.; Eder, B. Fully coupled “online” chemistry with the WRF model. *Atmos. Environ.* **2005**, *39*, 6957–6975. [[CrossRef](#)]
22. Menut, L.; Tuccella, P.; Flamant, C.; Deroubaix, A.; Gaetani, M. The role of aerosol-radiation-cloud interactions in linking anthropogenic pollution over southern west Africa and dust emission over the Sahara. *Atmos. Chem. Phys.* **2019**, *19*, 14657–14676. [[CrossRef](#)]
23. Thomas, B.; Viswanadhapalli, Y.; Srinivas, C.V.; Dasari, H.P.; Attada, R.; Langodan, S. Cloud resolving simulation of extremely heavy rainfall event over Kerala in August 2018—Sensitivity to microphysics and aerosol feedback. *Atmos. Res.* **2021**, *258*, 105613. [[CrossRef](#)]
24. Lompar, M.; Curic, M.; Romanic, D. Simulation of a severe convective storm using a numerical model with explicitly incorporated aerosols. *Atmos. Res.* **2017**, *194*, 164–177. [[CrossRef](#)]
25. Su, L.; Fung, C.H. Investigating the role of dust in ice nucleation within clouds and further effects on the regional weather system over East Asia—Part 1: Model development and validation. *Atmos. Chem. Phys.* **2018**, *18*, 8707–8725. [[CrossRef](#)]
26. Glotfelty, T.; Alapaty, K.; He, J.; Hawbecker, P.; Song, X.; Zhang, G. The Weather Research and Forecasting Model with Aerosol-Cloud Interactions (WRF-ACI): Development, Evaluation, and Initial Application. *Mon. Weather Rev.* **2019**, *147*, 1491–1511. [[CrossRef](#)]
27. Niranjana Kumar, K.; Ouarda, T.B.M.J. Precipitation variability over UAE and global SST teleconnections. *J. Geophys. Res. Atmos.* **2014**, *119*, 10313–10322. [[CrossRef](#)]
28. Wehbe, Y.; Ghebreyesus, D.; Temimi, M.; Milewski, A.; Al Mandous, A. Assessment of the consistency among global precipitation products over the United Arab Emirates. *J. Hydrol. Reg. Stud.* **2017**, *12*, 122–135. [[CrossRef](#)]
29. Wehbe, Y.; Temimi, M.; Ghebreyesus, D.T.; Milewski, A.; Norouzi, H.; Ibrahim, E. Consistency of precipitation products over the Arabian Peninsula and interactions with soil moisture and water storage. *Hydrol. Sci. J.* **2018**, *63*, 408–425. [[CrossRef](#)]
30. Steinhoff, D.F.; Brintjes, R.; Hacker, J.; Keller, T.; Williams, C.; Jensen, T.; Al Mandous, A.; Al Yazeedi, O.A. Influences of the Monsoon Trough and Arabian Heat Low on Summer Rainfall over the United Arab Emirates. *Mon. Weather Rev.* **2018**, *146*, 1383–1403. [[CrossRef](#)]
31. Branch, P.; Behrendt, A.; Gong, Z.; Schwitalla, T.; Wulfmeyer, V. Convection Initiation over the Eastern Arabian Peninsula. *Meteorol. Z.* **2020**, *29*, 67–77. [[CrossRef](#)]
32. Wehbe, Y.; Temimi, M.; Adler, R.F. Enhancing precipitation estimates through the fusion of weather radar, satellite retrievals, and surface parameters. *Remote Sens.* **2020**, *12*, 1342. [[CrossRef](#)]
33. Hulley, G.C.; Hook, S.J.; Abbott, E.; Malakar, N.; Islam, T.; Abrams, M. The ASTER Global Emissivity Dataset (ASTER GED): Mapping Earth’s emissivity at 100 meter spatial scale. *Geophys. Res. Lett.* **2015**, *42*, 7966–7976. [[CrossRef](#)]
34. Schwitalla, T.; Branch, O.; Wulfmeyer, V. Sensitivity study of the planetary boundary layer and microphysical schemes to the initialization of convection over the Arabian Peninsula. *Q. J. R. Meteorol. Soc.* **2020**, *146*, 846–869. [[CrossRef](#)]
35. Fonseca, R.; Francis, D.; Nelli, N.; Thota, M. Climatology of the Heat Low and the Intertropical Discontinuity in the Arabian Peninsula. *Int. J. Climatol.* **2021**, 1–26. [[CrossRef](#)]
36. Racz, Z.; Smith, R.K. The dynamics of heat lows. *Q. J. R. Meteorol. Soc.* **1990**, *125*, 225–252. [[CrossRef](#)]
37. Yu, Y.; Notaro, M.; Liu, Z.; Wang, F.; Alkolibi, F.; Fadda, E.; Bakhrjy, F. Climate controls on the interannual to decadal variability in Saudi Arabian dust activity: Toward the development of a seasonal dust prediction model. *J. Geophys. Res. Atmos.* **2015**, *120*, 1739–1758. [[CrossRef](#)]

38. Dumka, U.C.; Kaskaoutis, D.G.; Francis, D.; Chaboureau, J.-P.; Rashki, A.; Tiwari, S.; Singh, S.; Liakokou, E.; Mihalopoulos, N. The role of the Intertropical Discontinuity region and the heat low in dust emission and transport over the Thar desert, India: A premonsoon case study. *J. Geophys. Res. Atmos.* **2019**, *124*, 13197–13219. [CrossRef]
39. Rashki, A.; Kaskaoutis, D.G.; Mofidi, A.; Minvielle, F.; Chiapello, I.; Legrand, M.; Dumka, U.C.; Francois, P. Effects of Monsoon, Shamal and Levant winds on dust accumulation over the Arabian Sea during summer—The July 2016 case. *Aeol. Res.* **2019**, *36*, 27–44. [CrossRef]
40. Nelli, N.; Fissehay, S.; Francis, D.; Fonseca, R.; Temimi, M.; Weston, M.; Abida, R.; Nesterov, O. Characteristics of atmospheric aerosols over the UAE inferred from CALIPSO and Sun Photometer Aerosol Optical Depth. *Earth Space Sci.* **2021**, *8*, e2020EA001360. [CrossRef]
41. Bou Karam Francis, D.; Flamant, C.; Chaboureau, J.P.; Banks, J.; Cuesta, J.; Brindley, H.; Oolman, L. Dust emission and transport over Iraq associated with the summer Shamal winds. *Aeol. Res.* **2017**, *24*, 15–31. [CrossRef]
42. Kesti, J.; Backman, J.; O'Connor, E.J.; Hirsikko, A.; Asmi, E.; Aurela, M.; Makkonen, U.; Filioglou, M.; Komppula, M.; Korhonen, H.; et al. Aerosol particle characteristics measured in the United Arab Emirates and their response to mixing in the boundary layer. *Atmos. Chem. Phys.* **2021**. [CrossRef]
43. Dusek, U.; Frank, G.P.; Hildebrandt, L.; Curtius, J.; Walter, S.; Chand, D.; Drewnick, F.; Hings, S.; Jung, D.; Borrmann, S.; et al. Size Matters More Than Chemistry for Cloud-Nucleating Ability of Aerosol Particles. *Science* **2006**, *312*, 1375–1378. [CrossRef] [PubMed]
44. Hersbach, H.; Bell, B.; Berrisford, P.; Hirahara, S.; Horanyi, A.; Muñoz-Sabater, J.; Nicolas, J.; Peubey, C.; Radu, R.; Schepers, D.; et al. The ERA5 global reanalysis. *Q. J. R. Meteorol. Soc.* **2020**, *146*, 1999–2049. [CrossRef]
45. Olson, J.B.; Kenyon, J.S.; Angevine, W.A.; Brown, J.M.; Pagowski, M.; Suselj, K. *A Description of the MYNN-EDMF Scheme and the Coupling to Other Components in WRF-ARW*; NOAA Technical Memorandum OAR GSD61; National Center for Atmospheric Research: Boulder, CO, USA, 2019; 42p. Available online: <https://repository.library.noaa.gov/view/noaa/19837> (accessed on 16 September 2021).
46. Weston, M.; Chaouch, N.; Valappil, V.; Temimi, M.; Ek, M.; Zheng, W. Assessment of the Sensitivity to the Thermal Roughness Length in Noah and Noah-MP Land Surface Model Using WRF in an Arid Region. *Pure Appl. Geophys.* **2018**, *176*, 2121–2137. [CrossRef]
47. Zeng, X.; Beljaars, A. A prognostic scheme of sea surface skin temperature for modeling and data assimilation. *Geophys. Res. Lett.* **2005**, *32*, L14605. [CrossRef]
48. Temimi, M.; Fonseca, R.; Nelli, N.; Weston, M.; Thota, M.; Valappil, V.; Branch, O.; Wizemann, H.-D.; Kondapalli, N.K.; Wehbe, Y.; et al. Assessing the Impact of Changes in Land Surface Conditions on WRF Predictions in Arid Regions. *J. Hydrometeorol.* **2020**, *21*, 2829–2853. [CrossRef]
49. Thompson, G.; Eidhammer, T. A study of aerosol impacts on clouds and precipitation development in a large winter cyclone. *J. Atmos. Sci.* **2014**, *71*, 3636–3658. [CrossRef]
50. Nakanishi, M.; Niino, H. An improved Mellor-Yamada level 3-model: Its numerical stability and application to a regional prediction of advection fog. *Bound.-Layer Meteorol.* **2006**, *119*, 397–407. [CrossRef]
51. Nakanishi, M.; Niino, H. Development of an improved turbulence closure model for the atmospheric boundary layer. *J. Meteorol. Soc. Jpn.* **2009**, *87*, 895–912. [CrossRef]
52. Iacono, M.J.; Delamere, J.S.; Mlawer, E.J.; Shepherd, M.W.; Clough, S.A.; Collins, W.D. Radiative forcing by long-lived greenhouse gases: Calculations with the AER radiative transfer models. *J. Geophys. Res.* **2008**, *113*, D13103. [CrossRef]
53. Kain, J.S. The Kain-Fritsch convective parameterization: An update. *J. Appl. Meteorol.* **2004**, *43*, 170–181. [CrossRef]
54. Alapaty, K.; Herwehe, J.; Otte, T.L.; Nolte, C.G.; Bullock, O.R.; Mallard, M.S.; Kain, J.S.; Dudhia, J. Introducing subgrid-scale cloud feedbacks to radiation for regional meteorological and climate modeling. *Geophys. Res. Lett.* **2012**, *39*, L24809. [CrossRef]
55. Niu, G.-Y.; Yang, Z.-L.; Mitchell, K.E.; Chen, F.; Ek, M.B.; Barlage, M.; Kumar, A.; Manning, K.; Niyogi, D.; Rosero, E.; et al. The community Noah land surface model with multiparameterization options (Noah-MP): 1. Model description and evaluation with local-scale measurements. *J. Geophys. Res.* **2011**, *116*, D12109. [CrossRef]
56. Yang, Z.-L.; Yang, Z.-L.; Mitchell, K.E.; Chen, F.; Ek, M.B.; Barlage, M.; Kumar, A.; Manning, K.; Niyogi, D.; Rosero, E.; et al. The community Noah land surface model with multiparameterization options (Noah-MP): 2. Evaluation over global river basins. *J. Geophys. Res.* **2011**, *116*, D12110. [CrossRef]
57. Thompson, G.; Rasmussen, R.M.; Manning, K. Explicit forecasts of winter precipitation using an improved bulk microphysics scheme. Part I: Description and sensitivity analysis. *Mon. Weather Rev.* **2004**, *132*, 519–542. [CrossRef]
58. Thompson, G.; Field, P.R.; Rasmussen, R.M.; Hall, W.D. Explicit forecasts of winter precipitation using an improved bulk microphysics scheme. Part II: Implementation of a new snow parameterization. *Mon. Weather Rev.* **2008**, *136*, 5095–5115. [CrossRef]
59. Spyrou, C. Direct radiative impacts of desert dust on atmospheric water content. *Aerosol Sci. Technol.* **2018**, *52*, 693–701. [CrossRef]
60. Takenamura, T.; Nozawa, T.; Emori, S.; Nakajima, T.Y.; Nakajima, T. Simulation of climate response to aerosol direct and indirect effects with aerosol transport radiation model. *J. Geophys. Res.* **2005**, *110*, D02202. [CrossRef]
61. Saide, P.E.; Thompson, G.; Eidhammer, T.; da Silva, A.M.; Pierce, R.B.; Carmichael, G.R. Assessment of biomass burning smoke influence on environmental conditions for multiyear tornado outbreaks by combining aerosol-aware microphysics and fire emission constraints. *J. Geophys. Res. Atmos.* **2016**, *121*, 10294–20311. [CrossRef] [PubMed]

62. Ginoux, P.; Chin, M.; Tegen, I.; Prospero, J.M.; Holben, B.; Dubovik, O.; Lin, S.-J. Sources and distributions of dust aerosols simulated with the GOCART model. *J. Geophys. Res.* **2001**, *106*, 20255–20273. [[CrossRef](#)]
63. Colarco, P.; da Silva, A.; Chin, M.; Diehl, T. Online simulations of global aerosol distributions in the NASA GEOS-4 model and comparisons to satellite and ground-based aerosol optical depth. *J. Geophys. Res.* **2010**, *115*, D14207. [[CrossRef](#)]
64. Shettle, E.P.; Fenn, R.W. *Models for the Aerosols of the Lower Atmosphere and the Effects of Humidity Variations on Their Optical Properties*; Technical Report AFGL-TR-79-2014; Air Force Geophysical Laboratory: Dayton, OH, USA, 1979. Available online: <https://www.researchgate.net/publication/235074087> (accessed on 9 September 2021).
65. Ruiz-Arias, J.A.; Dudhia, J.; Gueymard, C.A. A simple parameterization of the shortwave aerosol optical properties for surface direct and diffuse irradiances assessment in a numerical in a numerical weather model. *Geosci. Model Dev.* **2014**, *7*, 1159–1174. [[CrossRef](#)]
66. Hodzic, A.; Duvel, J.P. Impact of biomass burning aerosols on the diurnal cycle of convective clouds and precipitation over a tropical island. *J. Geophys. Res. Atmos.* **2018**, *123*, 1017–1036. [[CrossRef](#)]
67. Stauffer, D.R.; Seaman, N.L. Use of four-dimensional data assimilation in a limited-area mesoscale model. Part I: Experiments with synoptic-scale data. *Mon. Weather Rev.* **1990**, *118*, 1250–1277. [[CrossRef](#)]
68. Stauffer, D.R.; Seaman, N.L.; Binkowski, F.S. Use of Four-Dimensional Data Assimilation in a Limited-Area Mesoscale Model Part II: Effects of Data Assimilation within the Planetary Boundary Layer. *Mon. Weather Rev.* **1991**, *119*, 734–754. [[CrossRef](#)]
69. Wooten, A.; Bowden, J.H.; Boyles, R.; Terando, A. The Sensitivity of WRF Downscaled Precipitation in Puerto Rico to Cumulus Parameterization and Interior Grid Nudging. *J. Appl. Meteorol. Climatol.* **2016**, *55*, 2263–2281. [[CrossRef](#)]
70. Durre, I.; Vose, R.S.; Wuertz, D.B. Overview of the Integrated Global Radiosonde Archive. *J. Clim.* **2006**, *19*, 53–68. [[CrossRef](#)]
71. Durre, I.; Xungang, Y. Enhanced radiosonde data for studies of vertical structure. *Bull. Am. Meteorol. Soc.* **2008**, *89*, 1257–1262. [[CrossRef](#)]
72. Banks, J.R.; Hunerbein, A.; Heinold, B.; Brindley, H.E.; Deneke, H.; Schepanski, K. The sensitivity of the colour of dust in MSG-SEVIRI Desert Dust infrared composite imagery to surface and atmospheric conditions. *Atmos. Chem. Phys.* **2019**, *19*, 6893–6911. [[CrossRef](#)]
73. Janowiak, J.; Joyce, B.; Xie, P. *NCEP/CPC L3 Half Hourly 4km Global (60S-60N) Merged IR V1*; Savtchenko, A., Ed.; Goddard Earth Sciences Data and Information Services Center (GES DISC): Greenbelt, MD, USA, 2017. [[CrossRef](#)]
74. Gelato, R.; McCarty, W.; Suarez, M.J.; Todling, R.; Molod, A.; Takacs, L.; Randles, C.A.; Darmenov, A.; Bosilovich, M.G.; Reichle, R.; et al. The Modern-Era Retrospective Analysis for Research and Applications, version 2 (MERRA-2). *J. Clim.* **2017**, *30*, 5419–5454. [[CrossRef](#)]
75. Roshan, D.R.; Koc, M.; Isaifan, R.; Shahid, M.Z.; Fountoukis, C. Aerosol Optical Thickness over Large Urban Environments of the Arabian Peninsula—Speciation, Variability, and Distributions. *Atmosphere* **2019**, *10*, 228. [[CrossRef](#)]
76. Ukhov, A.; Mostamandi, S.; da Silva, A.; Flemming, J.; Alshehri, Y.; Schevchenko, I.; Stenchikov, G. Assessment of natural and anthropogenic aerosol air pollution in the Middle East using MERRA-2, CAMS data assimilation products, and high-resolution WRF-Chem model simulations. *Atmos. Chem. Phys.* **2020**, *20*, 9281–9310. [[CrossRef](#)]
77. Koh, T.-Y.; Wang, S.; Bhatt, B.C. A diagnostic suite to assess NWP performance. *J. Geophys. Res.* **2012**, *117*, D13109. [[CrossRef](#)]
78. Reddy, N.N.; Rao, K.G. Contrasting variations in the surface layer structure between the convective and non-convective periods in the summer monsoon season for Bangalore location during PRWONAM. *J. Atmos. Sol.-Terr. Phys.* **2018**, *167*, 156–168. [[CrossRef](#)]
79. Evan, S.; Brioude, J.; Rosenlof, K.; Davis, S.M.; Holger, V.; Heron, D.; Posny, F.; Metzger, J.-M.; Duflot, V.; Payen, G.; et al. Effect of deep convection on the tropical tropopause layer composition over the southwest Indian Ocean during austral summer. *Atmos. Chem. Phys.* **2020**, *20*, 10565–10586. [[CrossRef](#)]
80. Beegum, S.N.; Gherboudj, I.; Chaouch, N.; Temimi, M.; Ghedira, H. Simulation and analysis of synoptic scale dust storms over the Arabian Peninsula. *Atmos. Res.* **2018**, *199*, 62–81. [[CrossRef](#)]
81. Cuesta, J.; Marsham, J.H.; Parker, D.J.; Flamant, C. Dynamical mechanisms controlling the vertical redistribution of dust and the thermodynamic structure of the West Saharan atmospheric boundary layer during summer. *Atmos. Sci. Lett.* **2009**, *10*, 34–42. [[CrossRef](#)]
82. Bou Karam, D.; Williams, E.; Janiga, M.; Flamant, C.; Cuesta, J.; Auby, A.; Thorncroft, C.; McGraw-Herdeg, M.; McGraw-Herdeg, M. Synoptic-scale dust emissions over the Sahara Desert initiated by a moist convective cold pool in early August 2006. *Q. J. R. Meteorol. Soc.* **2014**, *140*, 2591–2607. [[CrossRef](#)]
83. Francis, D.; Al Shamsi, N.; Cuesta, J.; Isik, A.G.; Dundar, C. Cyclogenesis and Density Currents in the Middle East and the Associated Dust Activity in September 2015. *Geosciences* **2019**, *9*, 376. [[CrossRef](#)]
84. Bou Karam, D.; Flamant, C.; Knippertz, P.; Reitebuch, O.; Pelon, J.; Chong, M.; Dabas, A. Dust emissions over the Sahel associated with the West African monsoon intertropical discontinuity region: A representative case-study. *Q. J. R. Meteorol. Soc.* **2008**, *134*, 621–634. [[CrossRef](#)]
85. Bou Karam, D.; Flamant, C.; Tulet, P.; Todd, M.C.; Pelon, J.; Williams, E. Dry cyclogenesis and dust mobilization in the intertropical discontinuity of the West African Monsoon: A case study. *J. Geophys. Res. Phys.* **2009**, *114*, D05115. [[CrossRef](#)]
86. Sarangi, C.; Kanawade, V.P.; Tripathi, S.N.; Thomas, A.; Ganguly, D. Aerosol-induced intensification of cooling effect of clouds during Indian summer monsoon. *Nat. Commun.* **2018**, *9*, 3754. [[CrossRef](#)] [[PubMed](#)]

87. Filioglou, M.; Giannakaki, E.; Backman, J.; Kesti, J.; Hirsikko, A.; Engelmann, R.; O'Connor, E.; Leskinen, J.T.T.; Shang, X.; Korhonen, H.; et al. Optical and geometrical aerosol particle properties over the United Arab Emirates. *Atmos. Chem. Phys.* **2020**, *20*, 8909–8922. [[CrossRef](#)]
88. Varghese, M.; Prabha, T.V.; Parade, S.; Gayatri, K.; Safai, D.; Axisa, D. Characteristics of CCN activation and cloud microphysics over the east coast of India during the Northeast Monsoon onset. *Atmos. Res.* **2021**, *257*, 105589. [[CrossRef](#)]
89. Wehbe, Y.; Tessendorf, S.A.; Weeks, C.; Bruintjes, R.; Xue, L.; Rasmussen, R.M.; Lawson, P.; Woods, S.; Temimi, M. Analysis of aerosol-cloud interactions and their implications for precipitation formation using aircraft observations over the United Arab Emirates. *Atmos. Chem. Phys.* **2021**, *21*, 12543–12560. [[CrossRef](#)]
90. Buchard, V.; Randles, C.A.; da Silva, A.M.; Darmenov, A.; Colarco, P.R.; Govindaraju, R.; Ferrare, R.; Hair, J.; Beyersdorf, A.J.; Ziemba, L.D.; et al. The MERRA-2 Aerosol Reanalysis, 1980 Onward. Part II: Evaluation and Case Studies. *J. Clim.* **2017**, *30*, 6851–6872. [[CrossRef](#)] [[PubMed](#)]
91. Wehbe, Y.; Temimi, M.; Weston, M.; Chaouch, N.; Branch, O.; Schwitalla, T.; Wulfmeyer, V.; Zhan, X.; Liu, J.; Al Mandous, A. Analysis of an extreme weather event in a hyper-arid region using WRF-Hydro coupling, station, and satellite data. *Nat. Hazards Earth Syst. Sci.* **2019**, *19*, 1129–1149. [[CrossRef](#)]
92. Fonseca, R.; Temimi, M.; Thota, M.S.; Nelli, N.R.; Weston, M.J.; Suzuki, K.; Uchida, J.; Kumar, K.N.; Branch, O.; Wehbe, Y.; et al. On the Analysis of the Performance of WRF and NICAM in a Hyperarid Environment. *Weather Forecast.* **2020**, *35*, 891–919. [[CrossRef](#)]
93. Sun, H.; Pan, Z.; Liu, X. Numerical simulation of spatial-temporal distribution of dust aerosol and its direct radiative effects on East Asian climate. *J. Geophys. Res.* **2012**, *117*, D13206. [[CrossRef](#)]
94. Fekih, A.; Mohamed, A. Evaluation of the WRF model on simulating the vertical structure and diurnal cycle of the atmospheric boundary layer over Bordj Badji Mokhtar (southwestern Algeria). *J. King Saud Univ. Sci.* **2019**, *31*, 602–611. [[CrossRef](#)]
95. Chaouch, N.; Temimi, M.; Weston, M.; Ghedira, H. Sensitivity of the meteorological model WRF-ARW to planetary layer schemes during fog conditions in a coastal arid region. *Atmos. Res.* **2017**, *187*, 106–127. [[CrossRef](#)]
96. Nelli, N.R.; Temimi, M.; Fonseca, R.M.; Weston, M.J.; Thota, M.S.; Valappil, V.K.; Branch, O.; Wulfmeyer, V.; Wehbe, Y.; Al Hosary, T.; et al. Impact of roughness length on WRF simulated land-atmosphere interactions over a hyper-arid region. *Earth Space Sci.* **2020**, *7*, e2020EA001165. [[CrossRef](#)]
97. Oke, T.R. *Boundary Layer Climates*, 2nd ed.; Routledge: London, UK, 1988; 464p.
98. Fountokis, C.; Ayoub, M.A.; Ackermann, L.; Perez-Astudillo, D.; Bachour, D.; Gladich, I.; Hoehn, R.D. Vertical Ozone Concentration Profiles in the Arabian Gulf Region during Summer and Winter: Sensitivity of WRF-Chem to Planetary Boundary Layer Schemes. *Aerosol Air Qual. Res.* **2018**, *18*, 1183–1197. [[CrossRef](#)]
99. Guo, J.; Yin, Y. Mineral dust impacts on regional precipitation and summer circulation in East Asia using a regional coupled climate system model. *J. Geophys. Res. Atmos.* **2015**, *120*, 10378–10398. [[CrossRef](#)]
100. Solmon, F.; Mallet, M.; Elguindi, N.; Giorgi, F.; Zayek, A.; Konare, A. Dust aerosol impact on regional precipitation over western Africa, mechanisms and sensitivity to absorption properties. *Geophys. Res. Lett.* **2008**, *35*, L24705. [[CrossRef](#)]
101. Chaboureaud, J.-P.; Cammas, J.-P.; Duron, J.; Mascart, P.J.; Sitnikov, N.M.; Voessing, H.-J. A numerical study of tropical cross-tropopause transport by convective overshoots. *Atmos. Chem. Phys.* **2007**, *7*, 1731–1740. [[CrossRef](#)]
102. Adebisi, A.A.; Kok, J.F. Climate models miss most of the coarse dust in the atmosphere. *Sci. Adv.* **2020**, *6*, eaaz9507. [[CrossRef](#)]
103. Kok, J.F.; Adebisi, A.A.; Albani, S.; Balkanski, Y.; Checa-Garcia, R.; Chin, M.; Colarco, P.R.; Hamilton, D.S.; Huang, Y.; Ito, A.; et al. Improved representation of the global dust cycle using observational constraints on dust properties and abundance. *Atmos. Chem. Phys.* **2021**, *21*, 8127–8167. [[CrossRef](#)]
104. Nelli, N.R.; Temimi, M.; Fonseca, R.M.; Weston, M.J.; Thota, M.S.; Vallapil, V.K.; Branch, O.; Wizeemann, H.-D.; Wulfmeyer, V.; Wehbe, Y. Micrometeorological measurements in an arid environment: Diurnal characteristics and surface energy balance closure. *Atmos. Res.* **2020**, *234*, 104745. [[CrossRef](#)]
105. Hansell, R.A.; Tsay, S.C.; Ji, Q.; Hsu, N.C.; Jeong, M.J.; Wang, S.H.; Reid, J.S.; Liou, K.N.; Ou, S.C. An Assessment of the Surface Longwave Direct Radiative Effect of Airborne Saharan Dust during the NAMMA Field Campaign. *J. Atmos. Sci.* **2010**, *67*, 1048–1065. [[CrossRef](#)]
106. Jimenez, P.A.; Dudhia, J.; Gonzalez-Rouco, J.F.; Navarro, J.; Montavez, J.P.; Garcia-Bustamante, E. A Revised Scheme for the WRF Surface Layer Formulation. *Mon. Weather Rev.* **2012**, *140*, 898–918. [[CrossRef](#)]
107. Lau, W.K.M.; Kim, K.M.; Shi, J.J.; Matsui, T.; Chin, M.; Tan, Q.; Peters-Lidard, C.; Tao, W.K. Impacts of aerosol-monsoon interaction on rainfall and circulation over Northern India and the Himalaya Foothills. *Clim. Dyn.* **2017**, *49*, 1945–1960. [[CrossRef](#)] [[PubMed](#)]
108. Grabowski, W.W. Separating physics impacts from natural variability using piggybacking technique. *Adv. Geosci.* **2019**, *49*, 105–111. [[CrossRef](#)]